Evolution model for the Absheron Mud Volcano: from stratified sediments to fluid mud generation

Arthur Blouin[1,2,3], Nabil Sultan[1], Alexandra Pierron[1], Patrice Imbert[3], Jean-Paul Callot[3]

[1] Ifremer, Lab. Aléas Géologiques et Dynamiques Sédimentaires, Géosciences Marines, REM, Centre de Bretagne, Pointe du Diable, 29280 Plouzané.

[2] R&D/EP Total S.A., Avenue Larribau, 64000 Pau.

[3] Université de Pau et des Pays de l'Adour, E2S UPPA, CNRS, TOTAL, Avenue de l'Université, 64013 Pau cedex, France

Corresponding author: Arthur Blouin (a.blouin@fugro.com)

Key Points:

- Simulation of mud generation is possible through regional 2D-diffusion modeling
- Mud ascent through gas-expansion-driven density inversion is possible, although additional processes may accelerate the phenomenon.
- Numerical modeling results allow proposing a semi-quantitative formation model for the Absheron mud volcano.

Abstract

We propose a semi-quantitative model of the initiation and early evolution of a mud volcano. Basin modeling was calibrated against our previous seismic interpretation of the Absheron mud volcano and surroundings in the South Caspian Basin on the one hand, analysis of geological samples from seabed and two exploration boreholes on the other. Some input parameters of the model were derived from laboratory testing of samples from the mud volcano and we used a constitutive law obtained from a previous laboratory study showing the extent to which gas exsolution may damage host sediments, eventually leading to mud generation from compacted sediments. The study identified key geological and physical conditions that led to mud volcano formation: coupling diffusion processes with hydrofracturing and fluid advection, we were able to simulate conditions required to generate mud 3.5 km below the Absheron mud volcano. We also modeled mud remobilization up to the seabed using Navier-Stokes equations modified to account for the impact of gas expansion on mud density. Considering density inversion only, simulations indicate that mud would be extruded at the seabed 100 years after its generation, an ascent rate similar to extrusion rates measured at some active mud volcanoes in Azerbaijan, e.g. the Kotyrdag mud volcano. These models considering eruption dynamics provide semi-quantitative support to purely conceptual formation models based on seismic interpretation of subvolcanic stratal geometry.

Plain language Summary

We propose an initiation and early evolution model of an active mud volcano based on previous observations, laboratory measurements and coupled numerical models. We built the model upon our previous geological and geophysical interpretation of the Absheron mud volcano in the South Caspian Basin, adding laboratory measurements on geological samples from the mud volcano and its subsurface strata. New laboratory experiments indicate that gas bubble growth in porous sediment disaggregates it into homogeneous mud. Our modeling of subsurface pressure and fluid circulation evolution indicates that the presence of natural flow baffles is paramount to generate mud below the mud volcano through bubble growth. Another model based on fluid mechanics evaluated the impact of bubble growth on mud density and simulated mud ascent to the seafloor. It suggests that eruption would happen 100 years after mud generation at depth, a velocity similar to those measured on onshore mud volcanoes expelling viscous mud. The new formation model integrates basin-scale fluid flow and eruption dynamics and quantifies physical parameters required to trigger and sustain mud volcano formation.

1. Introduction

While extensive work has focused for decades on mud volcano (MV) architecture and on gassy sediment structure and behavior, few studies have numerically explored MV formation and evolution. Several authors have attempted to reproduce, through analogue models, field as well as subsurface observations and suspected morphological evolution of MVs (Dupuis, 2017; Mourgues et al., 2012; Nermoen et al., 2010; Odonne et al., 2020; Woolsey et al., 1975). The results provide understanding of the evolution of surface structures and morphology as well as exploring possible subsurface mechanisms responsible for the observed data. However, most of these models used non-cohesive materials to simulate fine-grained cohesive sediments (Dupuis, 2017; Nermoen et al., 2010; Woolsey et al., 1975), following the theory on scaled models (Hubbert, 1937). The processes used to remobilize material in the models may be different from those applying to natural MVs. Other authors developed numerical models to explain the subsurface mechanism and simulate the remobilization of mud (Brown, 1990; Collignon et al., 2018a; Gisler, 2009; Zoporowski & Miller, 2009). These models are based on physical, chemical and mechanical laws applied to natural conditions, therefore approaching processes more accurately. However, these numerical models only assess the flow of fluid mud or the mechanical evolution of mud during its ascent. Deville et al. (2010) computed regional fluid flow models in the Barbados prism and showed that MVs are located above overpressured zones. Therefore, modeling of mud volcanoes focused on reproducing the observed structures or the mud flow dynamics, while other studies looked into the regional background to explain MV location. To our knowledge, none of the previous models integrated both the regional and local processes into a unique model. The impact of gas exsolution and expansion on subsurface sediment mobilization has been inferred from geophysical observations (Brown, 1990; Imbert et al., 2014; Lafuerza et al., 2012; Lawrence & Cartwright, 2010; Riboulot et al., 2013), but the physics of gas-related mud generation commonly ignored or simplified.

The AMV has been densely surveyed for hydrocarbon exploration purposes and for geohazard assessment (Contet & Unterseh, 2015; Dupuis, 2017; Gautherot et al., 2015; Unterseh & Contet, 2015) giving a dense and high-quality multidisciplinary dataset. The SCB is also densely studied, and several basin modeling integrating subsidence, thermal regime and petrophysical properties of formations to reconstruct fluid flow over geological time provide understanding of regional scale phenomena (Bredehoeft et al., 1988; Deville et al., 2010; Grosjean et al., 2009; Javanshir et al., 2015). Overall, existing data present a unique opportunity to model and simulate the formation of a mud volcano within its geological background. Previous modeling work carried out by Blouin et al. (2019a) aimed to explain the location of the AMV at the crest of the Absheron anticline, coupling sedimentation-related overpressure generation and 2D-diffusion equations for fluid flow and methane diffusion. It showed that the AMV was formed at the location where critical overpressure (near-fracture conditions) affected methane-saturated areas. However, hydrofracturing conditions were not reached solely through sedimentation and with the considered geological structure.

The present work assesses the following and complementary main questions:

- Is it possible to simulate mud generation conditions at depth by considering mechanical properties of sediments, sedimentation rates, structural elements and the impact of gas exsolution?
- Is the sole impact of gas expansion on the mud properties able to drive mud up to the seafloor?

Hereafter, we present the improvements brought to the 2D-diffusion model presented by Blouin et al. (2019a) by considering a low-permeability interval corresponding to the Anhydritic Surakhany Formation and by integrating fracture generation conditions, gas exsolution and sediment damage (Blouin et al., 2019b) ; these make it possible to propose a possible geological and physical setting and a chain of processes leading to mud generation. Modified Navier-Stokes equations accounting for gas bubble expansion and changes in mud properties (density and pressure) were used in order to simulate mud ascension through the sedimentary strata.

2. Material and methods

In addition to published data, we constrained the models using information from two exploration wells (pressure, stratigraphy) and subsurface geometry from the interpretation of a 3D seismic volume (Blouin et al., 2019a) and using laboratory testing results showing the impact of gas exsolution on the mechanical properties of compacted sediments (Blouin, et al., 2019b).

2.1. Mud generation

The method used to characterize sediment properties (including compressibility and hydraulic conductivities) of the modelled stratigraphic layers was already discussed in the companion paper (Blouin et al., 2019a). The software used to calculate the sedimentation-related overpressure (SeCoV3 Ifremer in-house software) is also described (Blouin et al., 2019a) and no further developments were done in the following modeling work.

The geometrical model, based on work by Green et al. (2009), was slightly modified (Figure 1) to take into account the Anhydritic Surakhany Formation (ASF, Blouin et al., 2019a). The fault network geometry is based on seismic interpretation (Blouin et al., 2019a).

The 2D-diffusion method was modified from the initial version described in the companion paper (Blouin et al., 2019a) in order to consider two additional phenomena: hydrofracturing and gas compressibility and exsolution (Boyle's and Henry's laws). In a context where the maximum principal effective stress is vertical ($\sigma'_1 = \sigma'_v$), hydrofracturing is vertical and occurs when and where the fluid pressure exceeds the sum of the tensile strength of the host sediment and the minimum horizontal stress (σ_3). For the purpose of modeling, a realistic approximation is to consider that hydrofracturing occurs for a given ratio between overpressure and vertical effective stress ($\Delta u/\sigma'_v$), generally obtained from pressure logs (see Blouin et al., 2019a). When the ratio $\Delta u/\sigma'_v$ reaches this critical condition, hydrofractures are generated in the concerned area. As a working hypothesis, the hydrofractured area permeability is calculated from hydraulic conductivity laws (equation (2) in Blouin et al., 2019a) using a void ratio of 1. Methane diffusivity in the hydrofractured area is considered as being the same as in faults. Fracturing may trigger a decrease of overpressure in the fractured zone leading to a decrease in the saturation concentration and consequently to gas exsolution. Hence, the degree of gas saturation (S_g) after exsolution is calculated in the fractured area. The calculation follows Boyle's law (methane compressibility) and the dissolution/exsolution capacity of methane Henry's law (dissolution/exsolution capacity of methane), both being pressure and temperature dependent. Therefore, temperature distribution was calculated over the modeled sedimentary column. We estimated a thermal gradient from temperature measurements in the two exploration wells (16°C/km; Blouin et al., 2019a) and seafloor temperature from Diaconescu et al., (2001) at 5.85°C.

Several studies noted that during marine sediment sampling, the structure and mechanical properties of sediments are impacted by gas exsolution and expansion (DeGroot et al., 2010; Esrig & Kirby, 1977; Priest et al., 2014; Sultan et al., 2010, 2012). Sultan et al., (2012) determined that damage of sediments from the Gulf of Guinea through a decrease in preconsolidation pressure was directly linked to the degree of gas saturation. This decrease in preconsolidation pressure with increasing degree of gas saturation was already highlighted on other sediments by several studies (Hight et al., 2002; Lunne et al., 2001). Blouin et al. (2019b) observed the same behavior on sediments from the Absheron mud volcano, mud being generated for a degree of gas saturation of 38 %.

The degree of gas saturation is consequently used to calculate the impact of gas exsolution on sediment damage through the equation obtained from laboratory testing on the AMV sediments (Blouin, et al., 2019b):

$$\frac{\sigma'_{p2}}{\sigma'_{p0}} = \exp(-0.07.S_{gmax}) \qquad (1)$$

with σ'_{p2} the preconsolidation pressure of sediments calculated after gas exsolution, σ'_{p0} the preconsolidation pressure of sediments before gas exsolution corresponding to the maximum vertical effective stress reached by the tested sample and S_{gmax} the maximum degree of gas saturation of the tested sample. Further details are available in Blouin et al. (2019b).

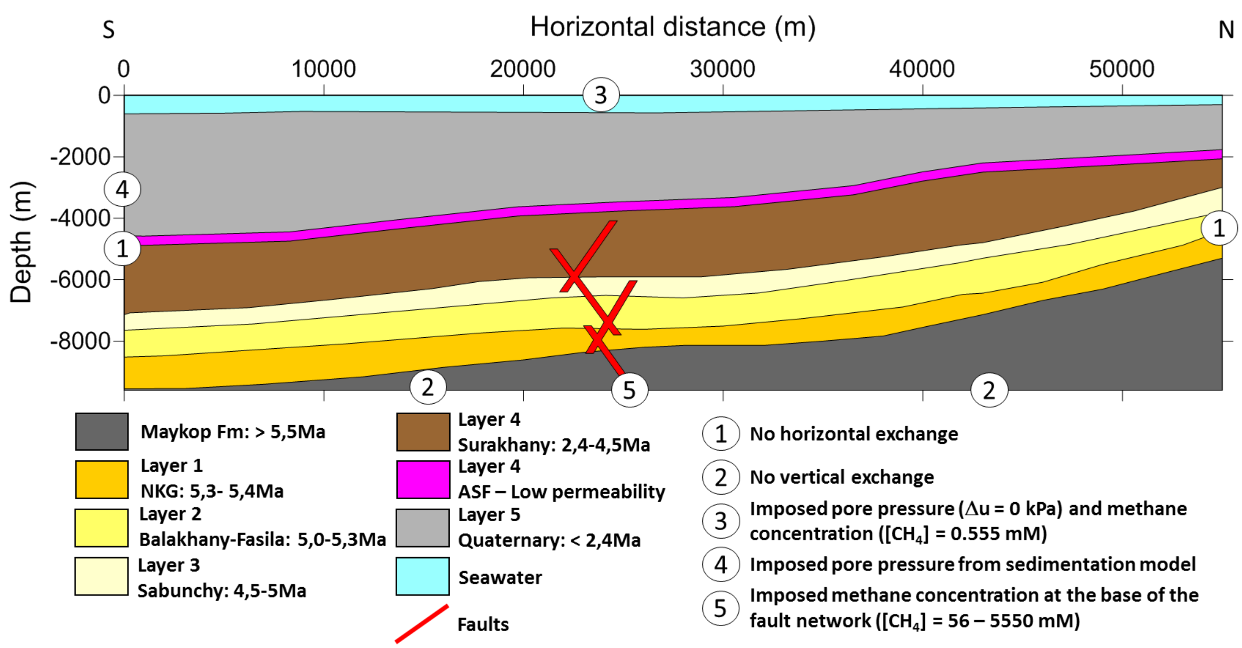

Figure 1: Updated geometry considering the ASF as a 300-meter-thick incompressible and low-permeability layer (purple). The limit conditions are similar to the model presented in the companion paper (Blouin et al., 2019a). However, condition 5 controlling the methane concentration injected at the base of the fault network is now considered as variable.

Methane and pore-pressure diffusion calculations may be initiated simulation stages accounting for hydrocarbon generation from mature source rocks since the beginning of Pliocene times, at the very beginning of the modeled sedimentation process. Boundary conditions are the same as those described and used in the companion paper (Blouin et al., 2019a) except for condition 5: the methane concentration imposed at the base of the fault network was considered between 56 and 5550 mM (Figure 1). In order to optimize the calculation time, the spatial resolution was reduced by considering a vertical resolution of 192 m with a total of 50 vertical nodes, and a horizontal resolution of 244 m with a total of 225 horizontal nodes (Figure 1).

Several tests were run on the hydraulic diffusivity (D_h) of the fault network, considering faults as either transmissive or sealing for lateral fluid flow based on regional studies and previous models (Battani et al., 2010; Bredehoeft et al., 1988; Caine et al., 1996; Evans et al., 1997; Gautherot et al., 2015; Gordon & Flemings, 1998; Javanshir et al., 2015; Wibberley et al., 2017).

2.2. Mud ascent

The numerical mud generation model is complemented by the modeling of the ascent of the fluid mud. The purpose of this model is to determine whether the mud mass is able to rise up to the seafloor through gas expansion processes only.

In order to model the mud flowing towards the surface, a fluid mechanics approach is commonly adopted using simplified Navier-Stokes equations (Collignon et al., 2018a; Gisler, 2009; Zoporowski & Miller, 2009).

In this work, we used the Tryggvason et al. (2006) model by including the effect of free gas expansion on the mud mass-density. More precisely, the software used in this paper is based on code1 of Tryggvason (2012). The code is freely available and free of use (Tryggvason, 2011). Navier-Stokes equations are governed by two basic equations. First, neglecting surface tension, taking gravity as sole body force and assuming constant and uniform viscosity, the momentum equation is given by Tryggvason et al. (2006) as:

$$\rho \frac{\partial u}{\partial t} + \rho \nabla . uu = -\nabla p + \rho g + \mu_0 \nabla^2 u \quad (2)$$

where ρ is the mass-density of the mud (kg/m^3), u is the fluid velocity (m/s), g is the gravitational acceleration (m/s^2), μ_0 is the viscosity considered as constant and uniform (Pa.s) and p is the fluid pressure (Pa) (Tryggvason et al., 2006).

Secondly, mass conservation for incompressible fluids is given by:

$$\nabla . u = 0 \quad (3)$$

as stated in Tryggvason et al. (2006).

One method for the resolution of this system of equations (Eq. (2) and Eq. (3)) is given by Tryggvason (2012). The momentum equation is integrated with time by splitting Eq. (2) into a velocity term and a pressure term, integrated separately. Then, each term of Eq. (2) is discretized using a Finite-Volume approach where both equations are applied over a small control volume. More details concerning the basic Navier-Stokes equations and the numerical methods are provided in Tryggvason (2012).

In the present work, we introduce the effect of gas on the mud mass-density through the following equation:

$$\rho = \phi(1 - S_g)\rho_w + (1 - \phi)\rho_s \quad (4)$$

Where ϕ is the porosity and ρ, ρ_w and ρ_s are the respective mass-densities of mud, water and solid particles. The density of free gas is considered as being negligible compared to the water mass-density and the mass-density of the solid particles. Gas solubility and compressibility are also calculated at each time step using Boyle's and Henry's laws.

We combined two approaches to model the ascent of low-density mud: one solving the problem in two dimensions at low viscosities (Tryggvason, 2012) and one for extrapolating the results to realistic higher viscosities using one-dimensional calculations (Furbish, 1997). The 2D calculations were completed using the Datarmor Ifremer supercomputer (PCDM, 2018) allowing to reduce significantly the time of calculation by parallel processing. Simulations that would need a week on a PC could be completed on less than 24 hours using the Datarmor supercomputer.

The 2D approach considers the mud as a one-phase fluid, whose flow was modeled using simplified Navier-Stokes equations (Eq. (2) and Eq. (3)), deriving gas compressibility from Boyles's law. Methane modifies the mass-density of the mud following Eq. (4) leading to mass-density inversion between the mud generation zone and the host rock (Brown, 1990; Collignon et al., 2018a; Deville, 2009; Kopf, 2002). Mud and host rocks are modelled as having the same viscosity, constant over time and that does not vary with the presence of free gas. The resolution method, using a discretization of the different terms of the simplified Navier-Stokes equations, was adapted from Tryggvason et al. (2011).

Two modified versions of code1 were tested. The modifications were made at Ifremer, for the purpose of the study. The first version (code1 v1) applies directly the numerical resolution method of Tryggvason (2012) by considering gas exsolution and expansion phenomena and by including in the computation the impact of free gas on the mass-density evolution. The second version (code1 v2) considers an initial mud overpressure due to the presence of free gas, which varies with the gas expansion during mud ascent.

The 2D simulation of mud ascent was completed over structural models with 100 x 100 nodes representing a 10-km-long and 4-km-thick section, corresponding to the approximate length of the Absheron anticline in a SSW-NNE direction and to the depth below sea level of the mud generation zone. The water column is considered and serves as an upper boundary limit where no exchange with the mud and sediment zones is allowed. Therefore, the extrusion of mud and its behavior after reaching the surface is not considered in the present work as it implies complex chemical and physical interactions between sea water and formation water (Etiope et al., 2009; Kopf, 2002). The two lateral boundaries are considered as no-exchange boundaries. The mass-density of the sediment decreases upward from 2100 kg/m^3 at the base of the model to 1900 kg/m^3 at the seabed. These values are calculated from porosities at wells, derived from sonic data (equation (3) in Blouin et al., 2019a) and using a grain solid mass-density of 2650 kg/m^3. An initial mud body is considered at the initial state corresponding to the volume of damaged sediments calculated from the regional diffusion simulation and having the same mass-density as unconsolidated marine sediments (1900 kg/m^3). In code1 v2, this initial volume of mud has also an initial overpressure which was obtained from diffusion simulations.

The mud generation process involves the formation of hydrofractures. These hydrofractures should propagate vertically in the context of the extrados of the Absheron anticline where normal faulting was observed. Therefore, vertical conduits having the same mass-density as the mud source can be introduced in the initial geometry in order to simulate the potential presence of vertical fractures.

Viscosities measured for surface marine sediments highly depends on the type of sediments, but are clearly below 10^{5} kPa.s (Jeong, 2013; Locat & Demers, 2008; Torrance, 2010). However, this range of values is not representative of highly consolidated and stratified sediments, whose typical values of viscosity exceed 10^{14} kPa.s, value corresponding to evaporitic sediments (Collignon et al., 2018a; Mukherjee et al., 2010). With the depth range and type of host sediment encountered here, taking realistic values would have led to exceedingly long computation times. The Lusi catastrophe provided the first direct monitoring of a mud volcano initiation (Mazzini et al., 2012; Tingay et al., 2017; Tingay et al., 2015). Tingay et al. (2017) proved using the BJP-1 well data and reports that the mud generation and its ascent from a depth of 1000 m happened within two days. Following these observations, we limited the simulations to the first 24 hours after the mud generation, leading to calculations time on the Datarmor supercomputer of more than 30 days for a viscosity of 10^{7} kPa.s. This directly arises from the resolution method: the time increment depends on the mesh resolution and on the viscosity. For instance, for a viscosity of 10^{7} kPa.s and for the used mesh of 100 x 100 nodes (mesh resolution of 100 m horizontally and 39 m vertically), a time increment dt of 10^{-5} s was needed in order to reach numerical convergence. This implies 1.7×10^{9} calculations to simulate the 24 hours of mud ascent. We therefore ran models based on Tryggvason (2012) over three orders of magnitudes for viscosity (10^{5}, 10^{6} and 10^{7} kPa.s) and observed that the main change was with the timing, other parameters of interest being insensitive to viscosity changes.

The extrapolation to more realistic viscosity values was completed by a simple 1D calculation following a simple example of Furbish (1997) modeling a buoyant magma flow within a vertical dyke. It was possible to calculate the velocity of the ascending mud using the equation:

$$v(x) = \frac{1}{2\mu}(\rho_c - \rho)g\left(r^2 - x^2\right) \quad (5)$$

with v the velocity of the ascending mud (m/s), μ the viscosity of the mud (kPa.s), ρ and ρ_c being the respective mass-densities of the mud and of the surrounding rock (reference) (kg/m^3), g the acceleration of gravity (m/s^2), r the radius of the mud chamber (m) and x the position relative to the center of the mud chamber (m). The mass-density of the reference rock was calculated just above the mud generation zone using the porosity obtained through the 2D sedimentation models and a mass-density for solid grains of 2650 kg/m^3. The degree of gas saturation was taken at 38 %, i.e. the limit for mud generation based on the laboratory testing by Blouin et al., (2019b). It allowed the calculation of the mud mass-density using Eq. (4). Therefore, applying Eq. (5), a maximum mud velocity was calculated for different sediment viscosities.

3. Results

3.1. Mud generation

3.1.1. One-dimensional sedimentation and pore pressure accumulation

The ASF is a 300-m-thick interval forming the uppermost interval of the Productive Series. It is comprised of a succession of evaporite beds and low resistivity shale intervals, some of which presented swelling behavior during drilling operations (Blouin et al., 2019a). It acts as an efficient seal, as overpressure rapidly builds up below this interval (Blouin et al., 2019a). The layer is therefore modeled as being incompressible ($C_C = 0$) and with a permeability reduced by one to two orders of magnitudes compared to other layers, and three orders of magnitude lower than the most permeable layer (Layer 4). Its sedimentation rate was taken equal to the one used for Layer 4, as being part of the same overall stratigraphic interval.

The presence of the low permeability ASF has prevented fluids from being expelled during the burial of the Productive Series. The increase in the overpressure gradient below the ASF described in the companion paper (Blouin et al., 2019a) clearly shows that fluids are trapped below the ASF, building-up the overpressure in the underlying strata. Therefore, the Upper PS might have kept an abnormally high porosity through compaction disequilibrium (Osborne & Swarbrick, 1997). Pressure data reported in Javanshir et al. (2015) as well as the reservoir overpressure values detailed in the companion paper (Blouin et al., 2019a) show that the Middle Productive Series and Lower Productive Series are drained through laterally continuous and connected reservoirs, which should have limited under-compaction in these intervals. Thus, in the following simulations Layer 4 permeability was artificially kept higher than in underlying and overlying intervals using a modified permeability law (Eq. (6)). That modified law reproduces the under-compaction caused by the ASF as displayed in Figure 2:

$$\ln(\mathrm{K}) = 3.06\ \mathrm{e} - 17.66 \qquad (6)$$

with K the hydraulic conductivity in m/s, and e the void ratio.

Using permeabilities obtained from oedometer tests and well data analysis (Blouin et al., 2019a), initial 1D properties were obtained from the deeper part of the section presented in Figure 1. We ran 13 iterations to estimate compaction-corrected deposition rates from the observed present-day thicknesses. The corrected sedimentation rates are summarized in Figure 2 and are quite similar to those obtained in the previous modeling work presented in the companion paper (figure 10 in Blouin et al., 2019a).

Figure 2 displays the main results of the 1D modeling that are taken as boundary condition 4 (Figure 1) in the 2D-diffusion models presented below. The results show the impact of the low-permeability ASF on overpressure that rises sharply when crossing this interval, accounting for the observed pressure build-up in well pressure logs (Blouin et al., 2019a). The low-permeability zone is well expressed in Figure 2 and contrasts with the high-permeability Layer 4. The overpressure slowly builds up over Layer 1, stays constant over Layer 4 and slightly increases over Layer 3, 2 and 1. The highest overpressure reached 40 MPa, which is in accordance with the pore pressure measured in the wells (Blouin et al., 2019a).

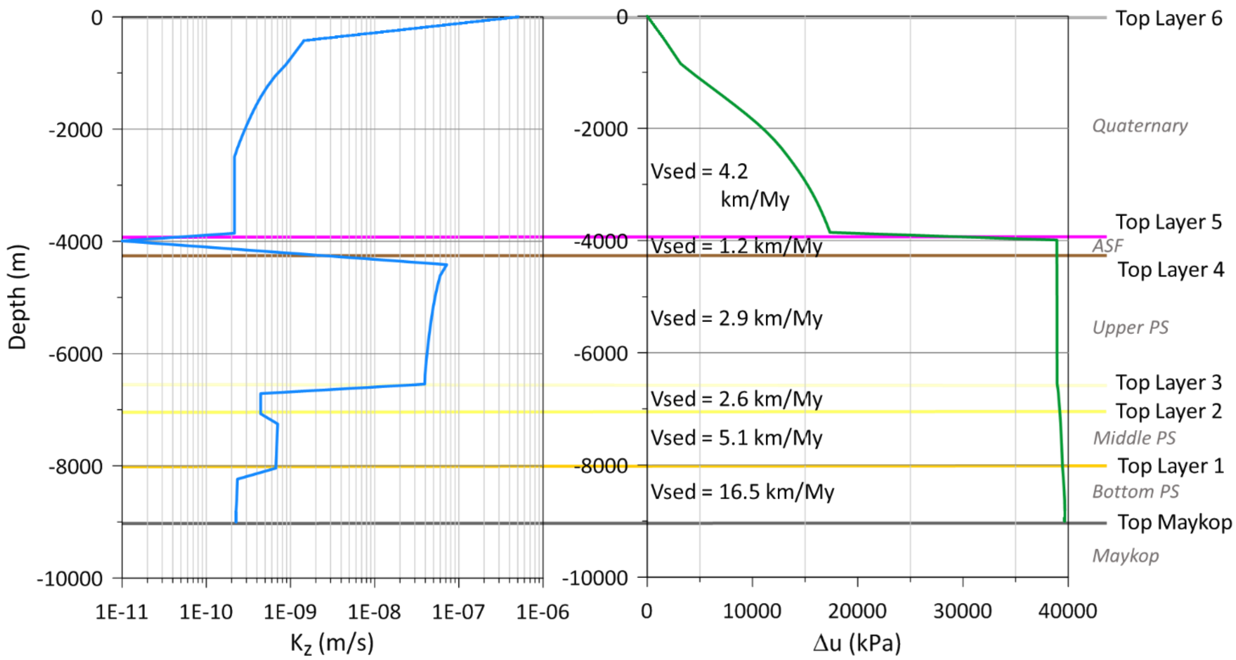

Figure 2: Results of the one-dimensional sedimentation modeling at the southern edge of the 2D geometrical model in Figure 1. On the left, vertical hydraulic conductivity versus depth trend at the end of the 5 My of sedimentation. On the right, overpressure versus depth trend at the end of the 5 My of sedimentation with corrected sedimentation rates for each layer. The top of each simulated stratigraphic unit is represented as indication using the same color code as in Figure 1 and the corresponding stratigraphic intervals are displayed in between.

3.1.2. Two-dimensional transient-diffusion processes, gas exsolution and damage

Four numerical simulations were conducted with different input parameters. The parameters used during the simulations are synthetized in Table 1. Most of the parameters are common for all the simulations and were obtained from literature and industrial reports (seafloor temperature, Henry methane constant) or from laboratory testing and well log interpretation (temperature gradient, sediment petrophysical properties; Blouin et al., 2019a). Four parameters were modified in order to fit observations and regional geology: fault hydraulic diffusivity, fracture condition, starting date for overpressure transmission, initial methane concentration.

Table 1: Parameters used for the different diffusion simulations presented in this study. Several parameters were modified to fit observations and regional background over the different simulations. e_0 is the initial void ratio, C_C is the compression index, T the temperature, K is the hydraulic conductivity (K_h in the horizontal direction, K_v in the vertical direction), D_h is the hydraulic diffusivity, D_C the methane molecular diffusivity, Δu is the overpressure, σ'_v is the vertical effective stress and e_{frac} the fracture void ratio.

		Simulation 1	Simulation 2	Simulation 3	Simulation 4
nodes number	vertically	50			
	horizontally	225			
Seafloor temperature		5.85°C			
grad(T)		16°C/km			
Henry methane constant		1.5×10^{-3} $M.atm^{-1}$			
fluid viscosity		1.15×10^{-6} kPa.s			
methane diffusivity		1.49×10^{-7} m^2/s			
e_0, C_C	Layer 6	2.734; 0.159			
	Layer 5, ASF	0.500; 0.000			

	Layer 4	2.014; 0.105			
	Layer 3	1.821; 0.094			
	Layer 2	1.643; 0.080			
	Layer 1	1.659; 0.081			
a, b, K_h/K_v K=exp(ae+b) (m/s)	Layer 6	3.064; -22.866; 2200.0			
	Layer 5, ASF	0.000; -25.328; 15.0			
	Layer 4	3.064; -17.666; 15.0			
	Layer 3	3.064; -22.150; 5.0			
	Layer 2	3.064; -21.803; 2.0			
	Layer 1	3.064; -22.333; 1.0			
e_0, C_C	faults	3.5; 0.0			
D_h (m²/s)	faults	5.5 x 10^{-6}	5.5 x 10^{-8}	5.5 x 10^{-8}	5.5 x 10^{-8}
D_C (m²/s)	faults	5.5 x 10^{-6} m²/s			
fracture condition: $\Delta u/\sigma'_v$		0.9	0.9	0.7	0.7
e_{frac}		1.0			
Start of overpressure diffusion (Ma)		1 My	1 My	1 My	3 My
Initial methane concentration (mM)		55.5	55.5	55.5	5550

i. Case 1: integration of the ASF layer properties

The 2D geometrical model, based on the work presented in Green et al. (2009), was modified in order to consider the impact of the low permeability of the ASF. The modeled geometry is displayed in Figure 1. The fracture condition $\Delta u/\sigma'_v$ was initially set at 0.9 given the mean fracture condition obtained from well data (Blouin et al., 2019a). Lateral overpressure transmission started 1 My after inception of methane diffusion in fault networks. Results of this simulation after 5 My are displayed in Figure 3. Methane diffusivity was set at 1.49 x 10^{-7} m²/s in sediments, and faults have a hydraulic diffusivity of 5.5 x 10^{-6} m²/s and a relatively high methane diffusivity coefficient of 5 x 10^{-4} m²/s in order to artificially include gas advection impact and create a preferential advective pathway for fluids.

Figure 3a shows overpressure diffusion across the structural model. Overpressure strongly increases below the ASF, reaching 38 MPa in the south of the model, and stays lower than 18 MPa above the ASF. Moreover, as Layer 4 is more permeable than the others, overpressure propagates more rapidly along this stratigraphic layer. Figure 3c shows the overpressure build-up below the ASF at the Absheron location that reaches 35 MPa over less than 1000 m. The main difference with results obtained without the ASF (figure 12 in Blouin et al., 2019a) is this clear and strong pressure build-up in Layer 4. The previous simulation calculated higher overpressure in Layer 5 (corresponding to Layer 6 in this paper), and overpressure increase with depth was more progressive.

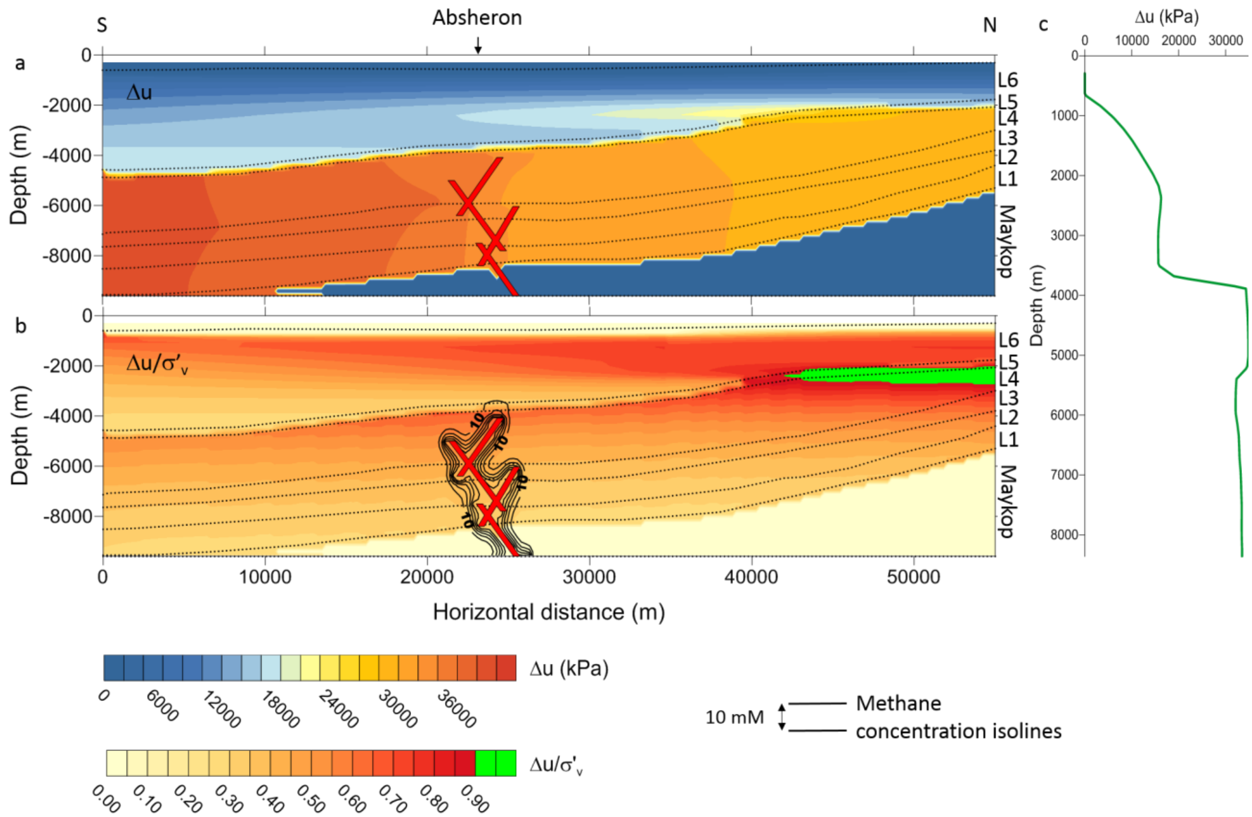

Figure 3: Results of overpressure and methane diffusion modeling after 5 My of calculation considering the low permeability ASF interval. Black dotted lines are for layer limits. Layer names are reported at the right of the sections. a: overpressure (Δu) in kPa after 5 My of migration through the structural model presented on Figure 1. Overpressure migrated more rapidly through layer 4 that has a higher permeability. b: $\Delta u/\sigma'_v$ contours with values exceeding hydrofracture condition below the ASF in the north of the model, where σ'_v is low. Black lines correspond to methane concentration contours. Lines are separated by 10 mM. c: Δu (kPa) vertical plot at the Absheron location (black arrow).

However, in terms of $\Delta u/\sigma'_v$ distribution, Figure 3b clearly shows that the maximum is reached just below the ASF, in the northern edge of the model where σ'_v is low due to thin overburden and probably to the boundary condition (Figure 1), which prevents lateral exchanges between the model and the outsides, therefore allowing overpressure build-up along the northern edge of the model. Hydrofracturing conditions are reached as $\Delta u/\sigma'_v$ is above 0.9 (green area in Figure 3b). No fracture conditions are reached at the Absheron location where calculated values do not exceed 0.7. Methane circulation is effective around the fault network showing that over 5 My, sediments get saturated with dissolved methane through the simulated transmissive fault network. The values of $\Delta u/\sigma'_v$ calculated here are higher than in the simulations described in the companion paper (figure 12 in Blouin et al., 2019a). The highest values are now localized below the ASF (Figure 3b) when they were distributed along the interval immediately above in the former version of the simulation (figure 12 in Blouin et al., 2019a). Methane distribution is similar to that of the former simulation (figure 12 in Blouin et al., 2019a) as the parameters for methane diffusivity were not modified.

Thus, the presence of the low permeability ASF allows reproducing pressure transmission and build-up mainly below this interval as well as reaching hydrofracturing conditions along the bottom end of the ASF. However, fractures open at the northern end of the structural model where σ'_v is lowest and where overpressure accumulates due to model boundary effects. Besides, no free gas, and consequently no sediment damage was observed due to fracture formation in an area where no dissolved gas was present.

ii. Case 2: sealing faults

The previous simulation shows that overpressure does not accumulate at the Absheron location but at the northern boundary of the model. Therefore, another simulation was conducted with modified boundary conditions. The pore pressure was drained at several levels below the ASF in order to dissipate overpressures in the north by setting Δu to zero. Hinds et al. (2004) and Javanshir et al. (2015) show that several sandstone intervals of the Productive Series are continuous and crop out onshore, especially in the lower PS. Therefore, the modeled hydraulic connection between the deeper part of the SCB and the surface, where atmospheric pressure prevails, does exist and was directly inferred from pressure logs at different well sites (Blouin et al., 2019a; Javanshir et al., 2015). However, the results of the simulation were inconclusive as overpressure was entirely dissipated at the north border of the model without any hydrofracturing in the calculation zone. Besides, the $\Delta u/\sigma'_v$ at the Absheron location did not change.

Thus, another working hypothesis was tested. Faults were initially set to create preferential pathways for fluids. Nevertheless, faults could be vertical pathways but horizontal seals for fluid circulation due to permeability anisotropy (Caine et al., 1996; Evans et al., 1997; Wibberley et al., 2008). Indeed, different authors noted in several regions around the world that faults may be sealing in the perpendicular direction but transmissive along the fault direction and that their permeability may vary depending on external parameters such as pore pressure, deformation style and the lithologies put in contact through the fault and within the fault itself (Henry et al., 2019; Morley et al., 2017; Wibberley et al., 2017). This feature was also already highlighted over the SCB and particularly in the Absheron anticline were gas was found in the northern flank while no economic gas accumulation was encountered in the southern flank (Gautherot et al., 2015; Grosjean et al., 2009; Javanshir et al., 2015). Several regional fluid flow numerical models already integrated fault anisotropy (Deville et al., 2010; Gordon & Flemings, 1998; Schneider et al., 2004). Besides, now that the ASF is modeled, slight corrections in the fault geometry are needed to fit the observations of the companion paper where the fault network ends in the ASF (figure 4 in Blouin et al., 2019a).

To simulate the horizontal sealing effect of the fault, the hydraulic diffusivity of the fault was taken equal to 5.5×10^{-8} m²/s. Vertical transmissivity was simulated by keeping a methane diffusivity of 5×10^{-4} m²/s. Results of this simulation are displayed in Figure 4.

Figure 4a displays the 2D distribution of overpressure after 5 My of calculation. The main feature is that with the sealing faults, overpressure builds up south of the faults, reaching 40 MPa, while in the northern part, the overpressure stays limited (around 18 MPa). The effect of the high permeability layer 4 contrasting with the low permeability ASF is still displayed with overpressure transmitting more rapidly along Layer 4 than in overlying intervals and with limited overpressure buildup in Layer 1. Figure 4c shows the overpressure profile with depth at the Absheron location. The sharp overpressure increase across the ASF and the weak overpressure gradient along Layer 1 are well captured by the model. Besides, an overpressure contrast is visible between Layer 4 and Layer 3 due to the effect of sealing faults, creating a trend similar to that observed in pressure logs at wells, with pressure horns and peaks (Blouin et al., 2019a).

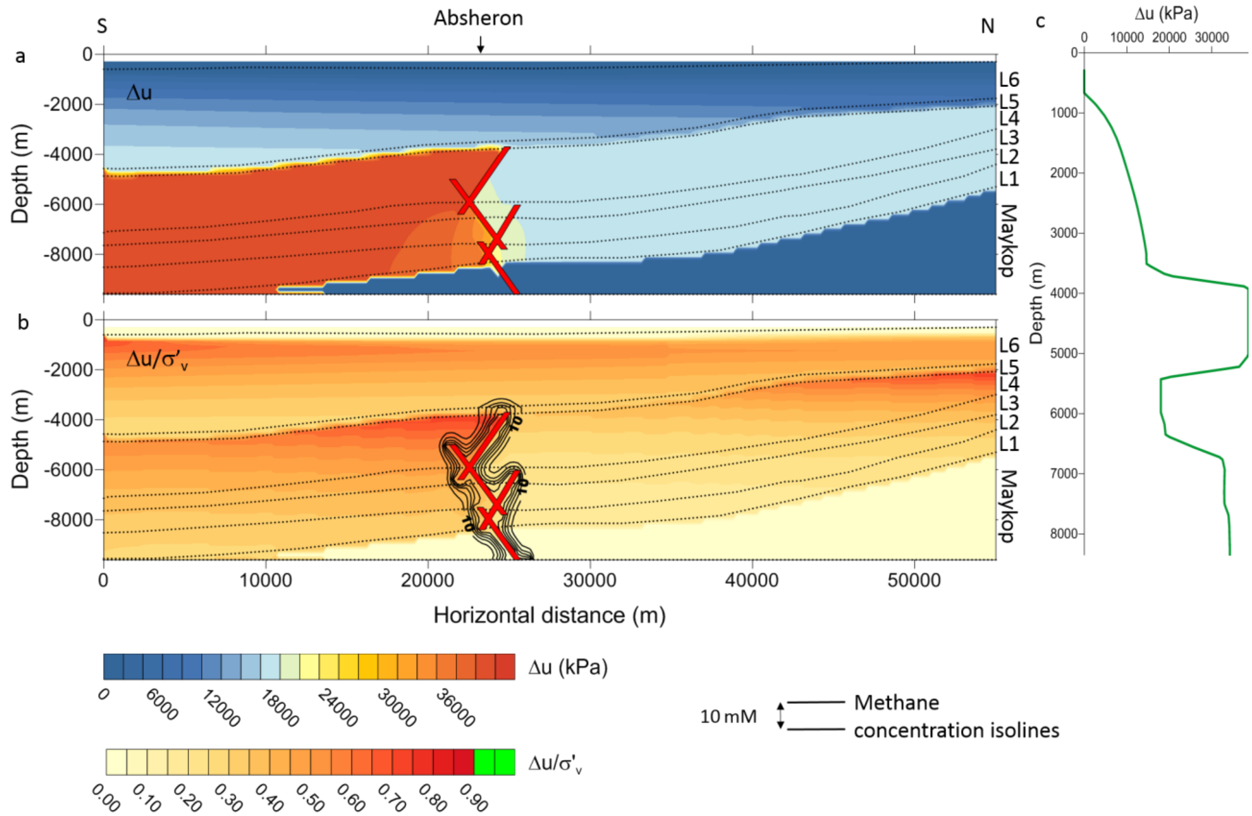

Figure 4: Results of overpressure and methane diffusion modeling after 5 My of calculation considering the low permeability ASF interval and faults as horizontal seals. Black dotted lines are for layer limits. Layer names are reported at the right of the sections. a: overpressure (Δu) in kPa after 5 My of migration through the structural model presented on Figure 1. Overpressure builds up along the fault network. North of the fault network overpressure is only of 18 MPa. b: $\Delta u/\sigma'_v$ contours. The highest values are now distributed south of the fault network, along the ASF, at the crest of the Absheron fold. Methane distribution is represented with black isolines, lines being separated by 10 mM. c: Δu (kPa) vertical plot at the Absheron location (black arrow).

High values of $\Delta u/\sigma'_v$ are now distributed in two main areas. To the north of the structural model where σ'_v is low and where some overpressure accumulated below the ASF, but most of all just south of the sealed fault network and along the ASF at the crest and along the southern flank of the Absheron anticline (Figure 4b). However, the fracture condition 0.9 is not reached, thus no fractures were created. The highest $\Delta u/\sigma'_v$ values reached are comprised between 0.70 and 0.75 (Figure 4b). Methane diffusion is similar to what was observed in the previous simulations as methane diffusivity of faults and sediments were not modified (Figure 4b). Methane concentrations are also the same.

Therefore, the fault network now acts as a seal for lateral pressure transmission and as a vertical pathway for fluids, allowing to approach critical conditions at the Absheron location.

iii. Case3: new assessment of fracture conditions

The fracture condition was previously set at 0.9 because of the mean value obtained on well data of the ratio between fracture pressure and overburden pressure. However, this value may be as low as 0.8 depending on the considered depth. Besides, at the time when the AMV started being active, sediments may have been less consolidated than at present which led to lower tensile strength hence lower hydrofracturing conditions. Therefore, a fracture condition of

0.7 was considered as plausible and is now considered in the following calculations. This value $\Delta u/\sigma'_v$ was already given as a minimum value for brittle failure of sedimentary rocks in several studies (Grauls & Baleix, 1994; Sibson, 2003).

A new calculation only changing the critical fracture criterion from 0.9 to 0.7 was carried out. Figure 5 synthetizes the results after 5 My of calculation.

Figure 5a and Figure 5c are roughly the same as Figure 4, as no changes were made that could affect directly the pressure field. Figure 5b shows that fracture condition was reached and that a fracture opened in the area of the Absheron anticline, south of the fault network, where $\Delta u/\sigma'_v$ is the highest. As fractures have a methane diffusivity of 5×10^{-4} m²/s, pore fluids migrated through the fractures along a horizontal plane, changing the distribution of the concentration of dissolved methane (Figure 5b). However, no gas exsolution occurred in this model, since the degree of gas saturation stayed at zero. This could be either due to the fact that the pressure drop through fracture was not high enough, or that the dissolved methane concentration is not sufficient, two parameters that control gas exsolution processes (Brown, 1990; Duan & Mao, 2006). Figure 5a and Figure 5c do not display any pressure decrease at fracture depth. As fractures are generated in an area where overpressure is constant, no drainage of fluids was possible, preventing pore pressure from a significant decrease. A vertical fracture that would have connected Layer 4 and Layer 6 through the ASF would have permitted a strong pressure decrease. Nevertheless, this was not possible since the ASF layer is characterized by a low-permeability coefficient impeding vertical pore pressure diffusion and therefore hydrofracturing.

Another important point is that hydrofracturing happened only 500,000 years after the beginning of pressure diffusion calculation, so 1.5 My after the beginning of the simulation. This shows that there is no need for calculating diffusion for a period as long as 5 My and that diffusion calculation could start at 3 Ma, date when all the PS were already deposited (Abreu & Nummedal, 2007; Forte & Cowgill, 2013; Green et al., 2009; Morton et al., 2003; Vincent et al., 2010). This could account for the deposition time of the main reservoirs, when hydrocarbon generation was already active (Guliyev et al., 2011; Inan et al., 2002; Smith-Rouch, 2006; Tagiyev et al., 1997).

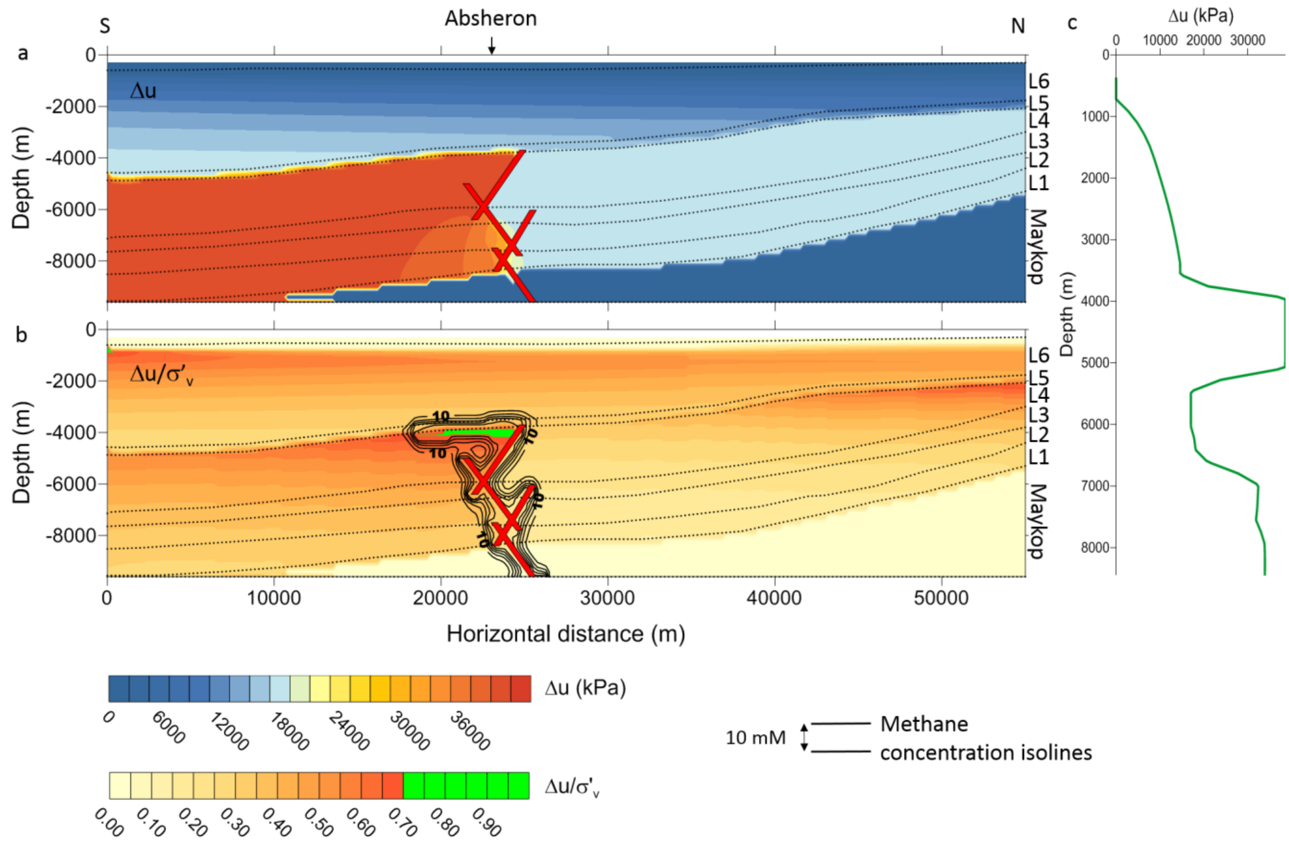

Figure 5: Results of overpressure and methane diffusion modeling after 5 My of calculation considering the low permeability ASF interval, faults as horizontal seals and a fracture condition of 0.7. Black dotted lines are for layer limits. Layer names are reported at the right of the sections. a: overpressure (Δu) in kPa after 5 My of migration through the structural model presented on Figure 1. b: $\Delta u/\sigma'_v$ contours. Fracture occurs along the bottom edge of the ASF, south of the fault network. Methane distribution is represented with black isolines, lines being separated by 10 mM. The dissolved methane distribution follows the fracture shape. c: Δu (kPa) vertical plot at the Absheron location (black arrow).

As a conclusion of this calculation, fractures were generated at the Absheron anticline crest, south of the fault network, and dissolved gas diffused into the fracture network. However, no free gas was formed because of either unsubstantial pressure decrease or low dissolved methane concentration.

iv. Case 4: high gas concentration at the base of the fault network

In order to test the impact of free gas at the fracture location (Figure 5b), the dissolved methane concentration of the fluid source at the bottom of the fault network (coming from a deeper source such as the Maykop source rock) was increased to 555 mM and to 5550 mM. The latter high methane concentration (twice higher than methane solubility at the entry point temperature and pressure conditions) imply the presence of free gas in addition to dissolved methane. However, this initial free gas volume which accumulates during several thousands of years, during sedimentation processes, is not supposed to cause any damage to the sediment as it would get dissolved as overburden increases. Here, damaging is considered to occur only during short-term exsolution process. The simulations start calculating pressure diffusion after 3 My of methane diffusion through the faults and the stratified sediment layers.

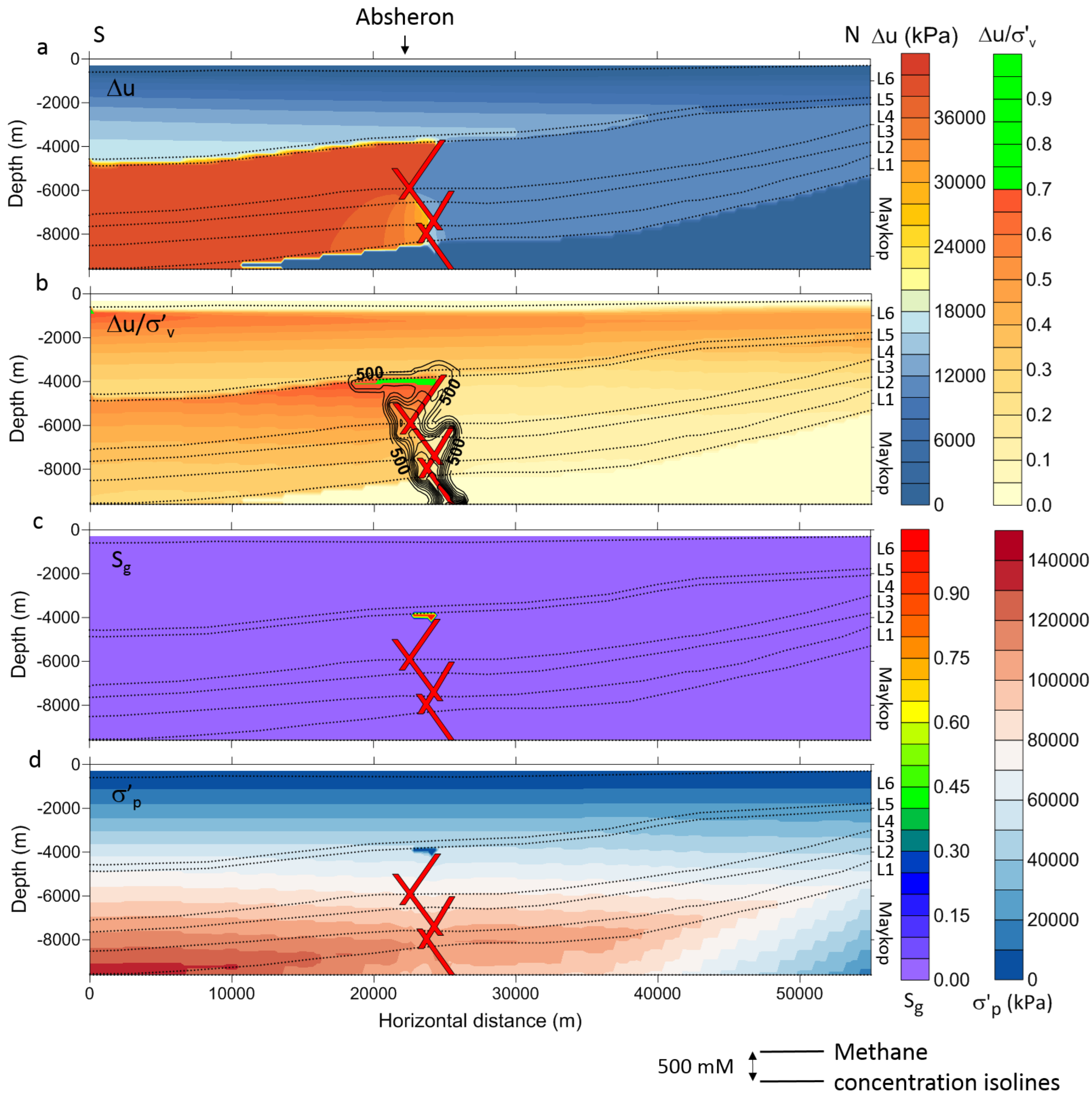

Figure 6: Results of the simulation considering the ASF, sealing faults, a fracture condition of 0.7 and an initial methane concentration of 5550 mM after 5 My. Black dotted lines are for layer limits. Layer names are reported at the right of the sections. a: overpressure (Δu) in kPa after 2 My of migration through the structural model presented on Figure 1. b: $\Delta u/\sigma'_v$ contours. Fracture occurs along the bottom edge of the ASF, south of the fault network. Methane distribution is represented with black isolines. The dissolved methane distribution follows the fracture shape and is depleted around fractures due to gas exsolution. c: degree of gas saturation (S_g) calculated after fracture formation. Values as high as 1 are reached in the central part of the fracture, in an area close to the fault network. d: preconsolidation pressure (σ'_p). It increases linearly with depth, but it is disturbed in the same area where gas exsolution happened reaching zero in the center of the fracture.

The simulation considering an initial methane concentration of 555 mM was not conclusive as the results obtained are the same in Figure 5. However, this showed that pore-pressure diffusion starting at 3 My does not impact the previous results.

Figure 6 shows the results of the simulation with an initial methane concentration of

5550 mM. Figure 6a shows that the overpressure field does not change compared to previous simulations. Figure 6b shows a similar $\Delta u/\sigma'_v$ distribution than in Figure 6b with a fracture generation below the ASF, south of the fault networks. The dissolved methane concentration follows faults and fractures but with higher concentrations, the lower value plotted being 500 mM (Figure 6b). Figure 6c displays the degree of free gas saturation (S_g) calculated across the structural model. S_g is above zero in an area corresponding to the fractured area close to the fault network and just below the ASF limit. Maximum values of 1 are reached in the center of the fractures. The model triggers gas exsolution locally after fracture generation for sufficient dissolved methane concentration.

Gas exsolution has a twofold effect. First, dissolved methane distribution is disturbed and partly depleted around the faults compared to the simulation proposed in Figure 5 (see Figure 6b) due to the fact that, locally, a part of the initially dissolved methane exsolved to form free gas. Moreover, as the simulation calculates the preconsolidation pressure (σ'_p), based on Eq. (1) (Blouin et al., 2019b) linking S_g with a preconsolidation ratio, we observe a local decrease in preconsolidation pressure in response to the presence of free methane (Figure 6d). This decrease in σ'_p is observed in the area where S_g is non-zero. σ'_p reaches almost 0 kPa where S_g is greater than 0.38, in areas where it was around 50 MPa before gas exsolution (Figure 6d).

Thus, this simulation considering 1- the presence of the ASF; 2- sealing faults; 3- a fracture condition of 0.7; and 4- an initial methane concentration of 5550 mM, was able to model sediment damage in an area just below the ASF and at the Absheron anticline crest, through fracture opening and the subsequent gas exsolution.

The integration of a low permeability layer corresponding to the ASF allowed transmitting overpressure into the Upper Productive Series and reaching critical overpressure conditions. The modification of fault hydraulic diffusivity in order to create horizontal seals resulted in critical conditions at the crest of the Absheron Anticline. These critical conditions created fractures that, coupled with sufficiently high dissolved methane concentration, allowed gas exsolution. Gas exsolution locally decreased the preconsolidation pressure of sediments sufficiently for them to lose all their initial structure. The observations made during the laboratory testing led by Blouin et al. (2019b) allow concluding that with the parameters used, conditions for mud generation are reached in the Upper Productive Series, at the Absheron mud volcano location.

3.2. Mud ascent

The approximate volume of mud and the initial geometrical conditions for mud ascent modeling were estimated from the previous calculations of the mud generation (Figure 6). The initial (2D) mud body for all simulations was set as a convex-up half-disc with a radius of 500 m, its base (diameter of the half-disc) being located 3400 m below seafloor with 500 m of water column above and centered on the horizontal axis of the model (Table 2). For code1 v2, the initial mud overpressure was set at 35 MPa, which is the pressure obtained in the mud generation zone at the end of the simulation presented in Figure 6. Mass-densities used for all simulations are indicated in Table 2.

Three values of the common viscosity of the ascending mud and host sediments were tested using both codes (with and without pressurized mud) as well as the impact of the presence of vertical conduits and of their length (Table 2).

Table 2: Parameters used in the different simulations completed during the study. The varying parameters are the sole sediment viscosity and the fracture length.

<table>
<tr><th rowspan="2">code version</th><th rowspan="2">viscosity (kPa.s)</th><th rowspan="2">conduit length (m)</th><th colspan="2">dimensions</th><th colspan="3">mud source</th><th colspan="4">Mass-densities (kg/m^3)</th></tr>
<tr><th>length</th><th>depth</th><th>dimension</th><th>position</th><th>overpressure</th><th>bottom</th><th>top</th><th>mud</th><th>Solid grains</th></tr>
<tr><td rowspan="9">code1 v1</td><td rowspan="3">10^5</td><td>0</td><td rowspan="18">10 km
100 nodes</td><td rowspan="18">3900 m
100 nodes</td><td rowspan="18">radius 500 m</td><td rowspan="18">x = 5000 m
z = 3900 m</td><td rowspan="9">No mud overpressure</td><td rowspan="18">2100</td><td rowspan="18">1900</td><td rowspan="18">1900</td><td rowspan="18">2650</td></tr>
<tr><td>1000</td></tr>
<tr><td>2000</td></tr>
<tr><td rowspan="3">10^6</td><td>0</td></tr>
<tr><td>1000</td></tr>
<tr><td>2000</td></tr>
<tr><td rowspan="3">10^7</td><td>0</td></tr>
<tr><td>1000</td></tr>
<tr><td>2000</td></tr>
<tr><td rowspan="9">code1 v2</td><td rowspan="3">10^5</td><td>0</td><td rowspan="9">35 MPa</td></tr>
<tr><td>1000</td></tr>
<tr><td>2000</td></tr>
<tr><td rowspan="3">10^6</td><td>0</td></tr>
<tr><td>1000</td></tr>
<tr><td>2000</td></tr>
<tr><td rowspan="3">10^7</td><td>0</td></tr>
<tr><td>1000</td></tr>
<tr><td>2000</td></tr>
</table>

3.2.1. Code1 v1

Figure 7 displays the results of the simulation for the median case, $\mu = 10^{6}$ kPa.s, using code1 v1. The initial state shows the initial geometry of the mud generation zone modeled as a 500 meters radius half-disc. The imposed mass-density is displayed, varying linearly from 1900 kg/m^3 at the seafloor to 2100 kg/m^3 at 3900 m. The mud mass-density is initially at 1900 kg/m^3. The degree of gas saturation (S_g) is initially 0 everywhere except in the mud generation zone where it is set at 0.38. The gassy-mud column starts rising after 3500 s. The changes in mass-density are mainly localized around the gassy-mud column and the velocity vectors are mainly disturbed in the immediate vicinity of the mud source reaching 0.04 m/s at 3750 s. The surrounding stratified sediments stay undisturbed, apart from the lateral edges where boundary conditions create some artifacts. As the degree of gas saturation increases due to methane expansion, the mass-density in the mud decreases (orange and green colors in Figure 8), triggering an acceleration of the process at 4500 s, when the gassy-mud column reaches 2200 m. The surrounding sediments are also impacted as the gassy-mud column rises, as non-negligible displacements are computed 2000 m away from the column with velocities reaching 0.1 m/s at 4500 s. The final stage (6000 s) shows that the gassy-mud column reaches the seafloor, with a width of 500 m. The corresponding mass-density of the gassy-mud column has values of 1450 kg/m^3 just below the seafloor. The gassy mud displays velocities of 0.25 m/s and surrounding sediments are disturbed significantly up to 3000 m away from the center of the model. The mass-density of the host sediment remains stable except near the model lateral boundaries due to computation artifacts. However, the initial stratification is preserved.

For μ = 10 ^{5} kPa.s (minimum case), the same observations are made but events occur 10 times faster. The initiation of mud ascent is observed after 350 s, and the final stage is reached after only 600 s. The velocity reaches 3.2 m/s in the ascending column and displacements are also visible in a radius of 3000 m around the center of the model. The stratification is also preserved and the ascending column is nearly 1 km wide. The mass-density is not disturbed around the gassy-mud column.

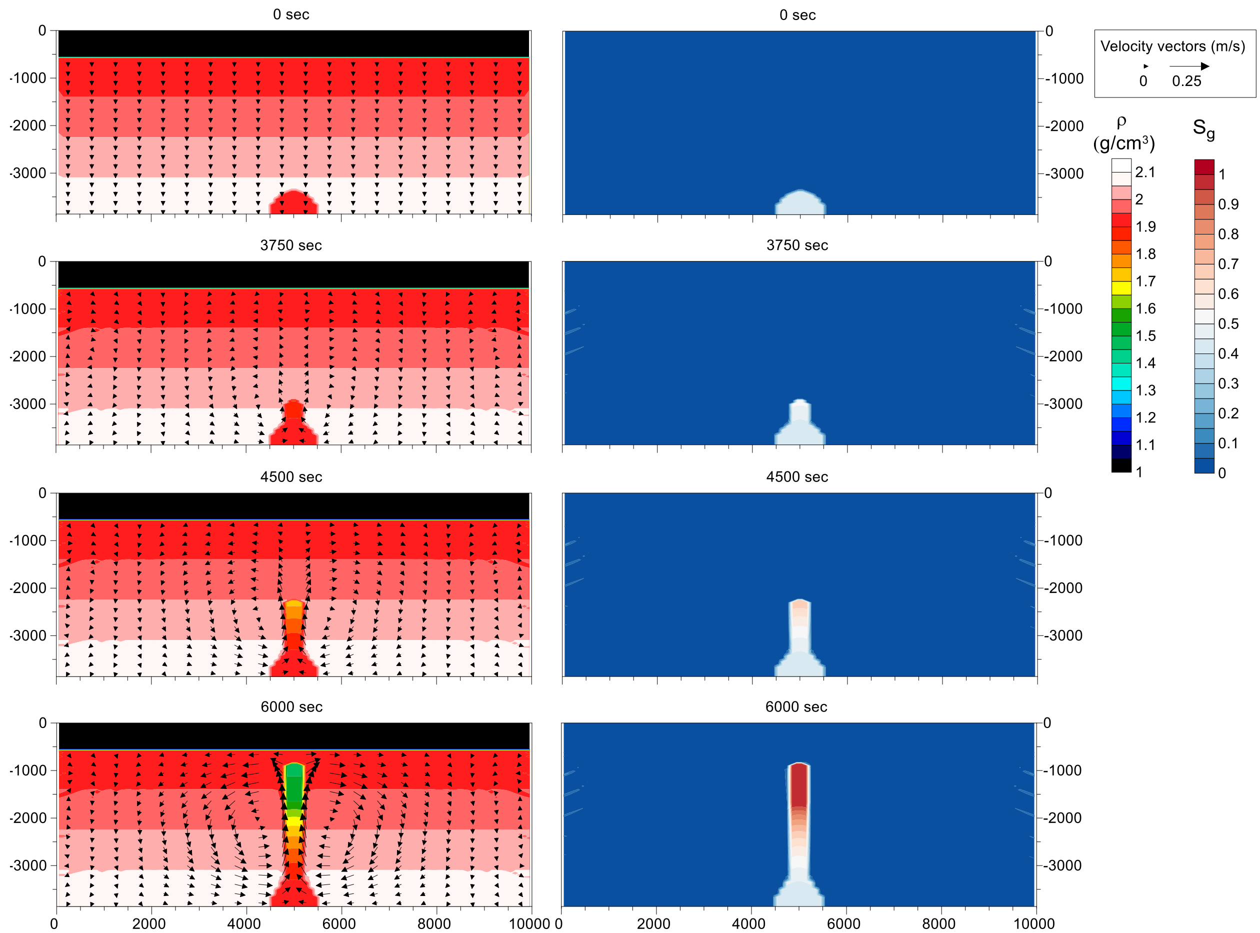

Figure 7: Results of the simulation using code1 v1 for μ = 10^{6} kPa.s. The left column displays the evolution of mass-density with time (left color scale) as well as the velocity vectors (m/s). The right column displays the evolution of the degree of gas saturation with time (right color scale).

For μ = 10 ^{7} kPa.s (maximum case), after 100,000 s, the gassy sediment column does not rise. We therefore tested the response of the simulation when a pre-existing conduit was added to the model (Table 2). As there are 100 nodes horizontally, it was not possible to center the vertical conduit, hence creating some dissymmetry in the results of simulations presented hereafter.

Two conduit lengths were tested: 1000 m and 2000 m from the base of the model (Table 2). The result of the simulation with μ = 10 ^{5} kPa.s and a 1000 m long vertical conduit is presented in Figure 8, where the conduit is displayed at the initial stage, with the same mass-density and the same degree of gas saturation as the mud generation zone. The initiation of gassy-mud ascent starts at 300 s. The gassy-mud ascent is mainly focused along the conduit, but it is superimposed with the normal gassy-mud ascent due to the presence of the mud source (as was observed without conduit). It is particularly visible as the conduit is not perfectly centered over the mud generation zone. The final stage is reached at 750 s. The final width of the gassy-mud column is 250 m. The velocity of the host sediments reaches 1.2 m/s at the direct proximity of the conduit and decreases to nil over a distance of 3 km. The timing of ascent conduit of 2-km conduit is very similar to the previous one, but the velocity only reaches 0.5 m/s, and the gassy-mud ascent is only focused above the vertical discontinuity, hence the final gassy-mud column is only 100 m wide.

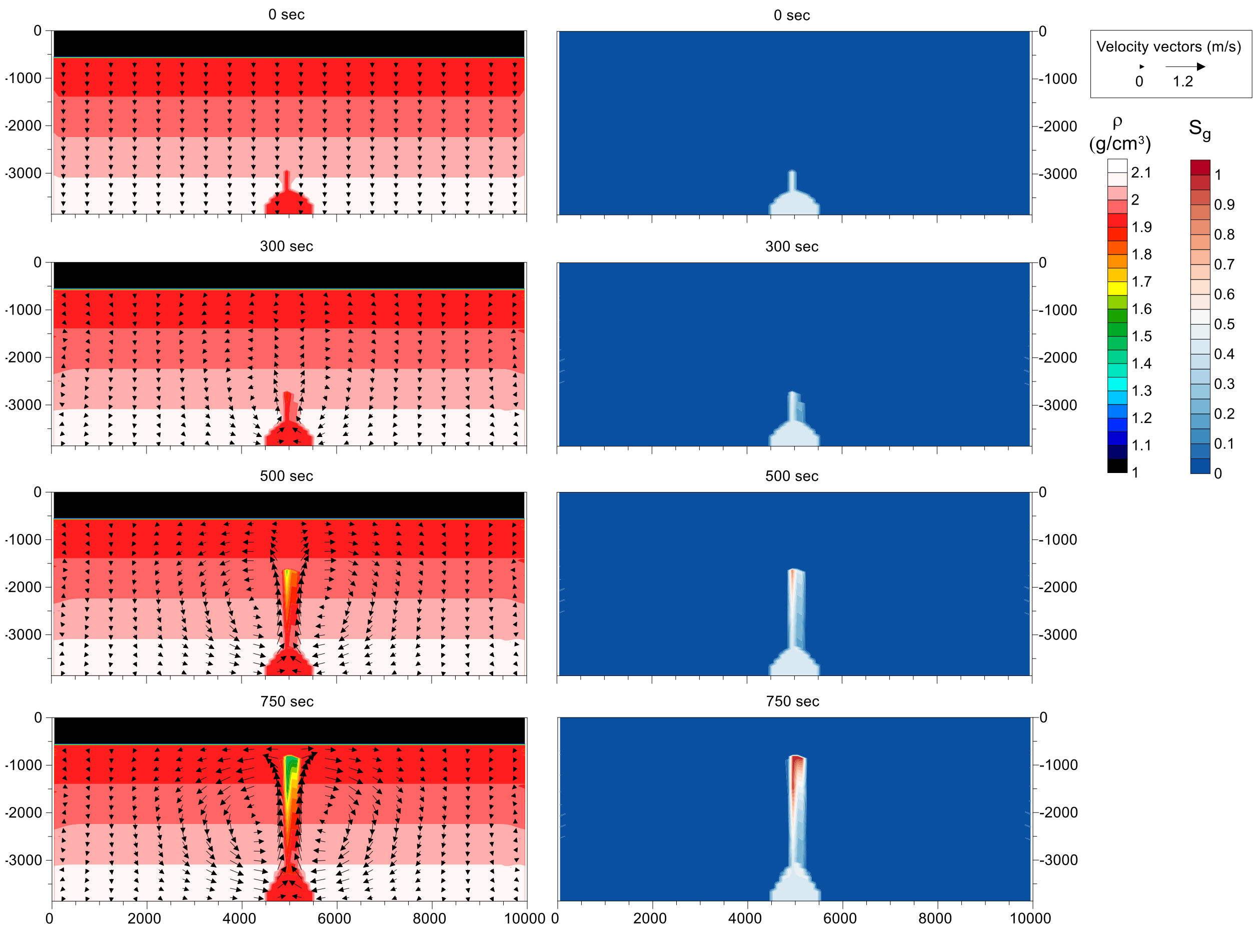

Figure 8: Results of the simulation using code1 v1 for μ = 10^5 kPa.s and a 1000 m long vertical conduit. The left column displays the evolution of mass-density with time (left color scale) as well as the velocity vectors (m/s). The right column displays the evolution of the degree of gas saturation with time (right color scale).

We also tested the impact of conduits for μ = 10^6 kPa.s. The results are overall similar to what has been described above with μ = 10^5 kPa.s, apart from the timing: initiation of gassy-mud ascent happens after 3000 s for both conduit lengths, and mud reaches the seafloor after 7000-7500 s. The maximum velocity is 0.12 m/s for a 1-km conduit and 0.05 m/s for a 2-km conduit conduit. The width of the gassy-mud column remains unchanged.

With μ = 10^7 kPa.s, even with 2 km-long conduits, no gassy-mud column was observed, even after 100,000 s, corresponding to over 3 weeks of computation time, exceeding the time limitation imposed on the Datarmor supercomputer.

3.2.2. Code1 v2

Code1 v2 considers the initial mud overpressure and its evolution with gas expansion. Fluid pressure in Eq. (2) is calculated separately through Boyle's law when free gas is present.

Figure 9 displays the results of the simulation for μ = 10 ^{6} kPa.s using code1 v2. The initial state is the same as in Figure 7. The different stages described for code1 v1 are the same with this version, but they occur earlier in the simulation. The ascending column initiates at 1750 s, and it is accompanied by a slight disruption in velocity vectors as shown in Figure 9 at 2000 s. This disruption increases as the ascending gassy-mud column rises, reaching 0.35 m/s in the ascending column at the final stage of the simulation and affecting a radius of 3000 m around the center of the model. The ascending column reaches the seafloor after 4000 s. A minimum mass-density of 1450 kg/m^3 is obtained at the top of the ascending column near the seafloor, 1000 m above the depth where the degree of gas saturation reaches 1. The ascending column is nearly 750 m wide at the final stage. The initial mass-density stratification is preserved as in Figure 7. Some computation artifacts due to the limit conditions of the model are still present.

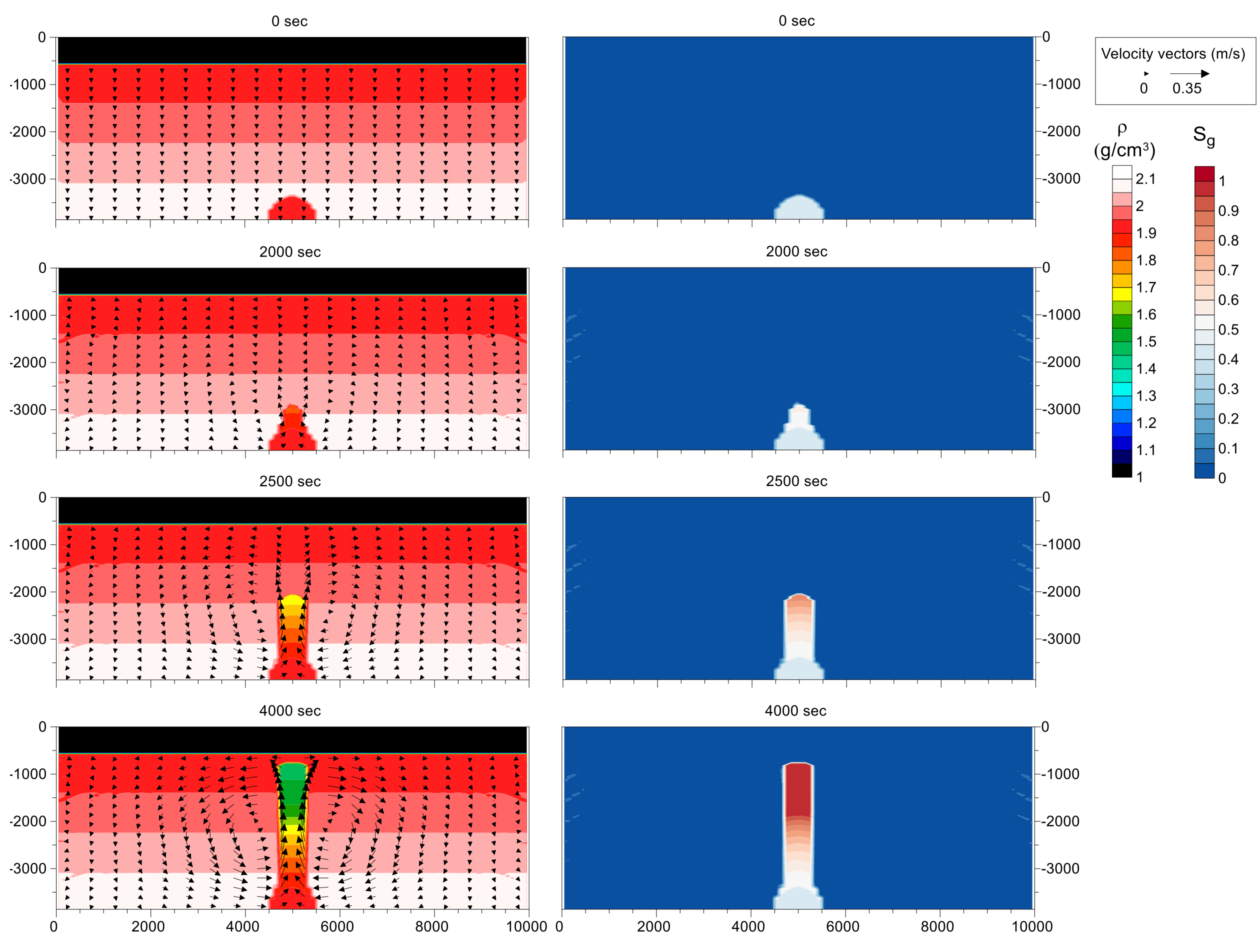

Figure 9: Results of the simulation using code1 v2 for μ = 10^6 kPa.s. The left column displays the evolution of mass-density with time (left color scale) as well as the velocity vectors (m/s). The right column displays the evolution of the degree of gas saturation with time (right color scale).

Again, for μ = 10 ^{5} kPa.s the same observations are made but 10 times earlier in the simulation than in Figure 9. The initiation of gassy-mud ascent is observed after 200 s, and the final stage is reached after only 400 s. The velocity reaches 3.5 m/s in the ascending column and displacements are also visible in a radius of 3000 m around the center of the model. The stratification is also preserved and the ascending column is also 750 m wide. The density is not disturbed near the column.

As observed earlier in code1 v1, for $\mu = 10^{7}$ kPa.s, after more than 10 days of computations, the simulation only reached 5000 s, and no initiation of an ascending column was visible. Further simulations with vertical discontinuities were made to understand the impact of conduits above the mud source (Table 2).

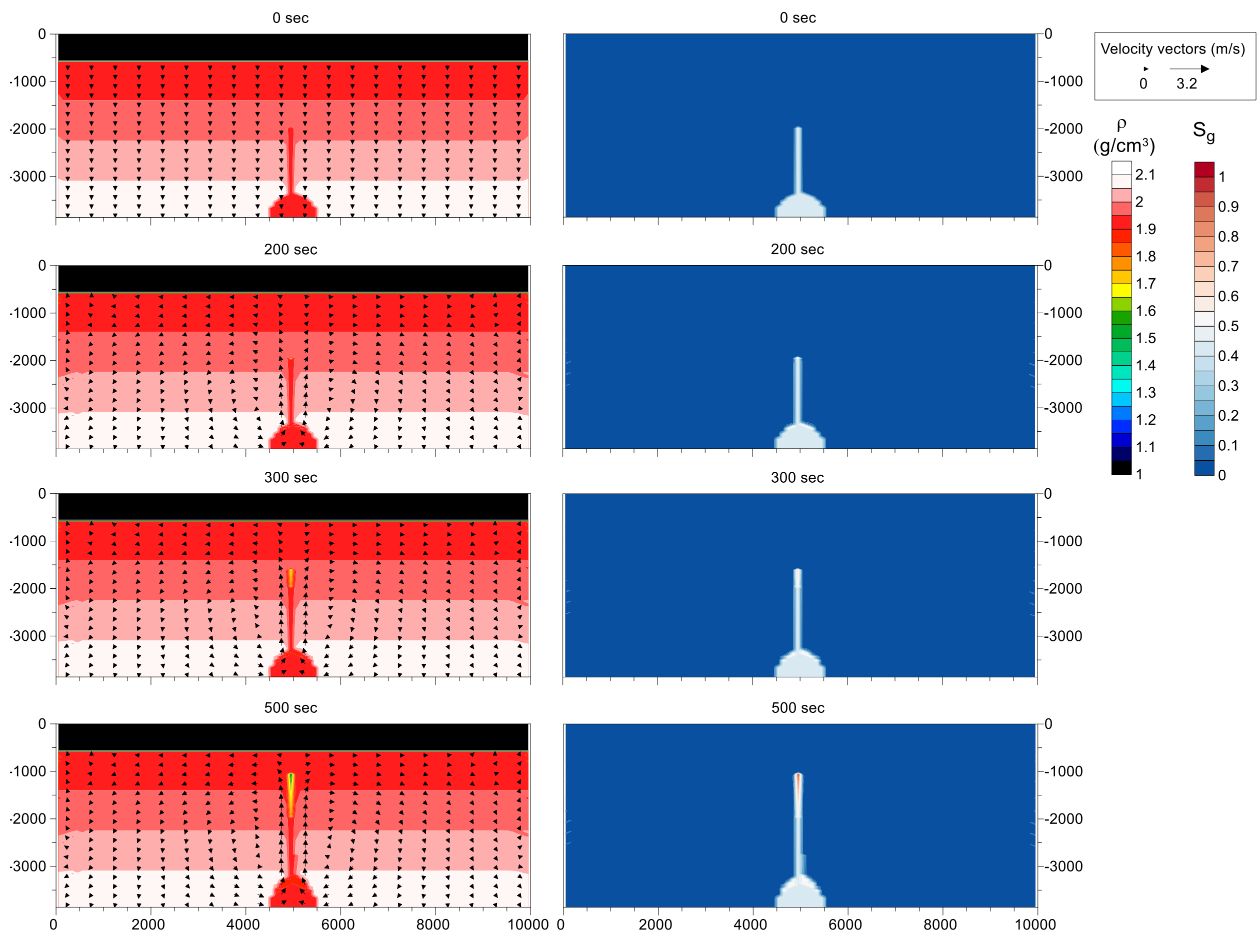

Figure 10: Results of the simulation using code1 v1 for $\mu = 10^{5}$ kPa.s and a 2000 m long vertical conduit. The left column displays the evolution of mass-density with time (left color scale) as well as the velocity vectors (m/s). The right column displays the evolution of the degree of gas saturation with time (right color scale).

At $\mu = 10^{5}$ kPa.s, the presence of a 1 km long vertical discontinuity generates similar effects to those obtained with code1 v1 and displayed in Figure 8. The gassy-mud column initiates at 200 s, mainly focusing along the conduit, but the direct impact of the mud generation zone is also visible (same as Figure 8). The column reaches the seafloor after 400 s, reaching 750 m in diameter and velocities of 4.2 m/s above the mud chamber. The velocity field is disturbed in a radius of 3 km around the conduit. The case of a 2-km conduit is displayed in Figure 10. An ascending gassy-mud column starts forming at 200 s just at the termination of the vertical conduit. The mud column gets larger at 300 s, forming a drop-shaped low-density area.

The gassy mud reaches the surface between 500 and 600 s with velocities reaching locally 3.2 m/s at the intersection between the conduit and the mud chamber. The gassy-mud column is 100 m wide at the end of the simulation.

This version of the code leads to computation times even longer than the first version, so no process initiation was observed for $\mu = 10^{7}$ kPa.s, even with 2 km-long conduits.

All the results obtained with the different 2D simulations discussed above are synthesized in Table 3. These results highly depend on the spatial and temporal resolution of the simulations, hence small variations are not considered to be relevant. It clearly shows that when viscosity increases by one order of magnitude, velocity decreases by one order of magnitude while the timing of initiation and extrusion increases by one order of magnitude (Table 3). When mud overpressure is considered in the simulations, it decreases the time for initiation and extrusion by a ratio of 0.65 to 0.5 (Table 3). The presence of vertical conduits above the mud chamber mainly influences the V_{max} which seems to decrease as the length of the conduit increases in the case of code1 v1 (Table 3). For code1 v2, V_{max} seems to remain roughly constant. The presence of a conduit also influences the final diameter of the gassy-mud column that decreases as the length of the conduit increases (Table 3).

Table 3: Synthesis of the main results obtained from the different simulations computed in this study. The initiation time of gassy-mud ascent, the time needed to reach the seafloor, the maximum velocity and the final diameter of the gassy-mud column are displayed for the two code versions.

code	μ (kPa.s)	Conduit length (m)	Initiation (s)	Extrusion (s)	Max. velocity (m/s)	Final diameter of gassy-mud column (m)
1 v1	10^5	0	350	600	3.2	1000
		1000	300	750	1.2	250
		2000	300	750	0.5	100
	10^6	0	3500	6000	0.25	500
		1000	3000	7000	0.12	250
		2000	3000	7500	0.05	100
	10^7	0	Computation too time consuming			
		1000				
		2000				
1 v2	10^5	0	200	400	3.5	750
		1000	200	500	4.2	400
		2000	200	500	3.2	100
	10^6	0	1750	4000	0.35	750
		1000	1500	4500	0.36	400
		2000	2000	4750	0.32	100
	10^7	0	Computation too time consuming			
		1000				
		2000				

3.2.3. Extrapolation to realistic viscosities: 1D calculations

In order to extrapolate the 2D simulation results obtained through the code modified from Tryggvason (2012), we tested simple 1D calculations based on the case of a buoyant magma flow along a vertical dyke (Furbish, 1997) in order to compare the velocities and timing obtained. Using Eq. (5) with r the radius of the mud chamber (r = 500 m) and taking x = 0 (maximum velocity above the center of the mud chamber) it was possible to obtain the maximum velocity above the mud chamber for varying viscosities. Figure 11a shows the results of 1D calculations of maximum velocities (V_{max}) for viscosities comprised between 10^{5} and 10^{12} kPa.s, considered as a valid approximation range for mud viscosities that are typically below the viscosity of sedimentary rocks. Two sets of models were run: the first one without initial mud overpressure (black), corresponding to the mud mass-density calculated through Eq. (4); the second (red line) considers an initial mud overpressure. Overpressure is limited to 78% of the effective stress (value of $\Delta u/\sigma'_v$ near the mud source at the end of 2D diffusion models; Figure 6), thus, the mass-density of mud was multiplied by 0.78 to take the mud overpressure into account. The maximum velocities obtained above the mud chambers for the 2D simulations without conduit are also plotted in Figure 11a. Figure 11b displays the same results in terms of minimum time for extrusion that was calculated considering that the velocity is V_{max} all along the conduit. The results in Figure 11b clearly show that the minimum time needed for the buoyant mud to reach the seafloor and form a mud volcano depends on mud viscosity.

One-dimension calculations show that the maximum velocity is inversely proportional to the viscosity (Figure 11a). Considering the initial mud overpressure, without modifying the viscosity, increases V_{max} by a factor 4.5, so that the two trends are parallel. For higher viscosities (10^{12} kPa.s), the maximum velocity is comprised between 10^{-6} and 10^{-7} m/s. Logically, the time for extrusion increases by an order of magnitude for each order of magnitude of μ (Figure 11b), a result which directly arises from the form of Eq. (5). The consideration of the mud overpressure allows reducing this time for extrusion. Therefore, for μ = 10^{12} kPa.s, it would take a minimum of 500 years for the buoyant mud to reach the surface if mud overpressure was not considered, while it only takes 100 years if mud overpressure is integrated in the calculation.

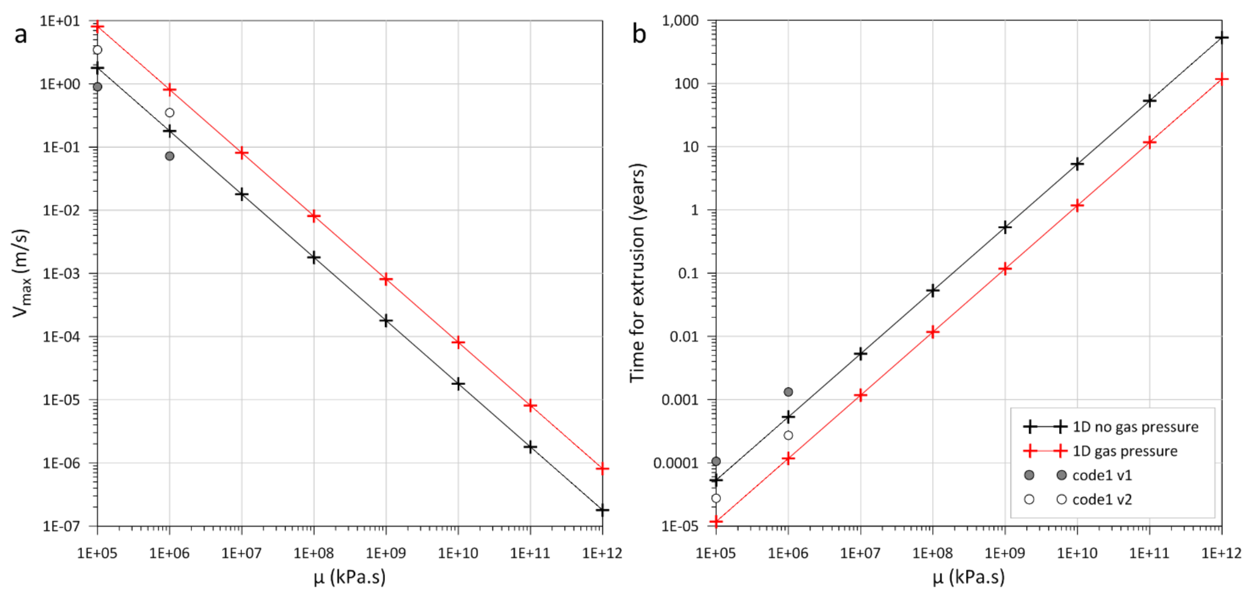

Figure 11: Results of 1D calculations based on the case of a buoyant magma flow along a vertical dyke presented in Furbish

(1997) considering a radius of 500 m corresponding to the mud source radius, compared to results obtained with 2D simulations. a: maximum velocity versus viscosity, b: minimum time for extrusion versus viscosity. Black lines with crosses correspond to the case where the initial mud overpressure is not considered, red lines are for the case with mud overpressure. Grey dots correspond to the results of the 2D simulations using code1 v1 and white dots the results of 2D simulations with code1 v2.

The 2D simulations results display the same relationship. μ and V_{max} are inversely proportional (Figure 11a). Considering the initial mud overpressure in code1 v2 leads to a 4-fold increase of V_{max} compared with code1 v1 (Figure 11a). Moreover, the values obtained with code1 v1 stands close to the black line (1D calculations without mud overpressure), and the values of code1 v2 are closer to the red line compared to code1 v1 results (1D calculations considering mud overpressure).

The same calculation was applied but in the case of a 50-m-wide conduit corresponding to the size of the conduits in the 2D simulations (Figure 12). The same relationship between μ and V_{max} and μ and the time for extrusion are displayed in Figure 12. The impact of mud overpressure seems to be limited as the difference between the V_{max} and the time for extrusion obtained considering mud overpressure and without mud overpressure is reduced compared to Figure 11. Moreover, V_{max} values extracted from 2D simulations are larger by nearly one order of magnitude than those obtained from 1D calculations (Figure 12a). Therefore, the time for extrusion is smaller by one order of magnitude (Figure 12b). Besides, the conduit width corresponds to the minimum that could be computed considering the model resolution, one node corresponding to 100 m and the conduit being computed over a unique node. Hence, the results displayed are not representative of the circulation that would occur in natural fractures whose width is much smaller.

From this 1D calculation, it arises that the time required for achieving extrusion, considering a viscosity of 10^{12} kPa.s, is significantly increased. Considering mud overpressure, it would take more than 10,000 years for the mud to reach the surface through thin fractures when it was 100 years for the calculation considering the mud chamber radius.

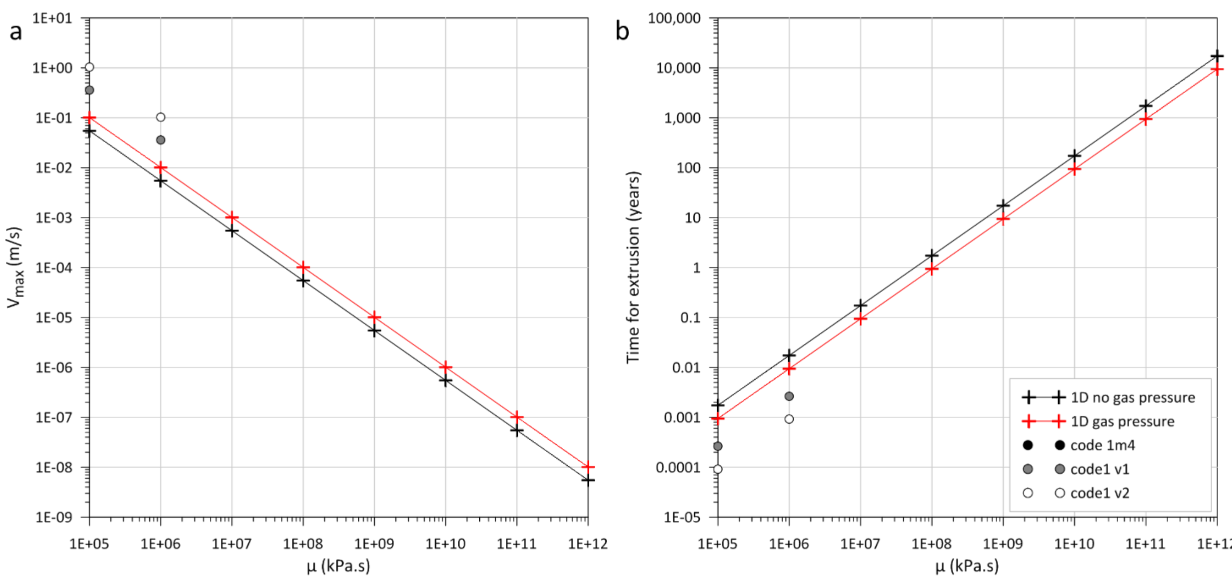

Figure 12: Results of 1D calculations based on the case of a buoyant magma flow along a vertical dyke presented in Furbish (1997) considering a radius of 50 m corresponding to the conduit width, compared to results obtained with 2D simulations. a: maximum velocity versus viscosity, b: time for extrusion versus viscosity. Black lines with crosses correspond to the case where the initial mud overpressure is not considered, red lines are for the case with mud overpressure. Grey dots correspond to the results of the 2D simulations using code1 v1 and white dots the results of 2D simulations with code1 v2.

4. Discussion

4.1. Synthesis of the main results

Representing the low-permeability Anhydritic Surakhany Formation (ASF) in the model generates a sedimentation-related overpressure contrast between layer 6 and deeper layers, thus reproducing the sharp overpressure increase observed in well-log data (Blouin et al., 2019a). Moreover, the model simulates maximum overpressure values of 40 MPa corresponding to the values measured in situ at the Absheron exploration wells (Blouin et al., 2019a). It also improved the preliminary 2D diffusion model presented in the companion paper (figure 12 in Blouin et al., 2019a) with overpressure now occurring essentially below the ASF and transmitted through Layer 4 (Figure 3). Overpressure diffusion started after 3 My of simulation, a duration corresponding to the deposition of the entire Productive Series interval. Lateral compartmentalization of the 2D model through the presence of faults having low horizontal permeability (Gautherot et al., 2015; Javanshir et al., 2015) was necessary to generate overpressure at the location of the AMV (Figure 4). Faults are commonly regarded as presenting permeability anisotropy, with the higher permeability along the fault surface (Caine et al., 1996; Deville et al., 2010; Evans et al., 1997; Henry et al., 2019; Morley et al., 2017; Schneider et al., 2004; Wibberley et al., 2008), thus methane-saturated water migration from the Maykop Fm. was provided by high methane diffusivity in faults, artificially simulating high vertical permeability accounting for advection processes. A new fracture condition of 0.7 based on pressure logs at well sites was adopted, which generated in the model a fractured area at the Absheron crest, just below the ASF (Figure 5). For an initial methane concentration of 5550 mM, gas exsolution was triggered in the fractured area resulting in a strong sediment damage in the fracture zone, with preconsolidation pressure locally approaching zero (Figure 6). From the results of the laboratory testing discussed by Blouin et al. (2019b) the improved 2D diffusion model simulated the mud generation zone formation below the Absheron MV.

To understand a possible ascent mechanism of the mud from its source to the seafloor, we based our approach on fluid mechanics using modified 2D Navier-Stokes equations considering the impact of gas expansion (Boyle's law) on the mass-density of the mud. Mud viscosities were limited to values between 10^{5} kPa.s and 10^{7} kPa.s because higher viscosities resulted in exceedingly long simulations. Results were then extrapolated with a simple 1D calculation to viscosities up to 10^{12} kPa.s. Results of the 2D simulations show that ascent velocity is inversely proportional to mud viscosity, while the time needed for mud ascent initiation and for mud extrusion is proportional to viscosity (Table 3). When mud overpressure is considered in the simulations, it decreases the time for initiation and extrusion by a ratio of 0.5-0.65 (Table 3). The presence of conduits mainly influences the final width of the gassy-mud column, which decreases with an increasing conduit length (Table 3). Through one-dimensional extrapolation it would take a minimum of 500 years for a buoyant high-viscosity mud to reach the surface if mud overpressure is not considered, while it would take only 100 years if the mud overpressure is integrated in the calculation (Figure 11b). Considering the radius of a conduit (Figure 12b), it arises that the timing for extrusion is significantly increased as it would take more than 10,000 years for the same overpressured mud to reach the surface. Combining 1D and 2D simulations, adapting the Navier-Stokes equations to consider the impact of gas expansion on sediment mass-density through Boyle's law and the influence of mud overpressure over the ascension velocity allowed estimating the time needed for mud generated at depth to reach the seafloor and to form a mud volcano through density-inversion.

In the following, the results of the calculations carried out in this paper will be discussed and confronted to previous research to assess the two main questions of the introduction:

- Is it possible to simulate mud generation conditions at depth by considering the mechanical properties of sediments, the sedimentation rates, structural elements and the impact of gas exsolution?
- Is the sole impact of gas expansion on the mud properties able to drive mud up to the seafloor?

4.2. Overpressure, hydrofracturing and gas exsolution: from stratified sediments to fluid mud

Calculations of pressure related to the maximum gas column that could have been trapped within the ASF (chapter 3, Blouin, 2019) showed that the sole presence of a gas reservoir at the crest of the Absheron fold cannot explain the formation of the Absheron mud volcano, as the fracture pressure was not reached. Hydrofracturing is believed to be necessary to initiate a MV formation as demonstrated through the monitoring of the Lusi initiation (Tingay et al., 2017) and through the analysis of the Absheron Mud Volcano dataset (Blouin et al., 2019a). Therefore, additional parameters are required to explain the AMV formation. The sedimentation rates recorded in the SCB are among the highest in foreland basins (Tagiyev et al., 1997; Allen et al., 2002; Smith-Rouch, 2006; Egan et al., 2009; Green et al., 2009). High sedimentation generates overpressure in low-permeability strata (Dugan & Flemings, 2000; Opara, 2011; Osborne & Swarbrick, 1997) and overpressure is one of the key triggers and drivers for MV formation (Deville, 2009; Dimitrov, 2002; Kopf, 2002; Mazzini & Etiope, 2017).

The 2-D diffusion model presented in this paper is based on regional data extracted from literature (Diaconescu et al., 2001; Green et al., 2009), on observations and in situ measurements made on the Absheron gas condensate field, as well as on the laboratory experiments conducted by (Blouin et al., 2019b). The regional-scale pressure gradient and northward fluid circulation from the deep SCB was already observed and discussed by several studies (Bredehoeft et al., 1988; Gautherot et al., 2015; Grosjean et al., 2009; Javanshir et al., 2015), and this type of modeling, studying the influence of regional physical parameters such as sedimentation rate and pressure gradient on local structures such as landslides or venting sites, has already been applied to other sedimentary basins (Dugan & Flemings, 2000; Schneider et al., 2004; Kvalstad et al., 2005; Hustoft et al., 2009). Deville et al. (2010) applied a similar fluid flow numerical model to show that MVs in Trinidad are located above overpressured areas. However, it is the first time, in our knowledge, that a 2D-diffusion model is applied to simulate sediment remobilization into mud at depth.

More precise measurements and estimations of layer permeability and fracture pressure would now be needed to improve this simulation. Laboratory testing on rock fragments from the different modeled layers would be necessary to improve their hydro-mechanical properties. Rock cores were sampled at well sites, but only from targeted reservoirs. Therefore, the shallower simulated intervals would already need approximations such as those from this study. Fracturing pressure was only estimated from pressure logs (Blouin et al., 2019a). However, LOT/FIT data indicate that hydrofracturing may occur for an overpressure of 25 MPa. Therefore, less than 2 My of overpressure diffusion may be necessary in our simulation in order to obtain the needed 25 MPa to trigger fracture generation as the fracture in Figure 6 generated for over 35 MPa of overpressure.

The simulation generated a horizontal fractured area where gas exsolved, locally reaching S_g greater than 0.38 and therefore damaging sediments that entirely lost their preconsolidation pressure. This area represents the mud generation zone and is 1300 m long and locally 220 m thick (Figure 6). The presence of the low-permeability ASF prevented pore pressure and therefore fractures to propagate vertically even if the maximum principal stress is vertical, the simulation ignoring the impact of compressive tectonics that are observed over the basin.

The 2D modeling presented in this study allows drawing a coupled process for mud generation below the AMV. Due to high sedimentation rates, overpressure is generated in the deeper part of the SCB and is transmitted northwards along under-compacted layers that kept an abnormally high permeability. The fault system at the core of the Absheron anticline leads to local overpressure build-up above the crest of the anticline, eventually initiating hydrofracturing and saturating the pore waters of the Upper Productive Series with methane. Hydrofracturing may trigger a local decrease in overpressure, allowing exsolution of the dissolved methane and triggering sediment damage when Sg exceeds 0.38 (Blouin et al., 2019b). Thus, the 2D diffusion model integrating the mechanical properties of sediments, sedimentation rates, compartmentalization effect of faults and regional seal and the impact of gas exsolution reproduces mud generation conditions at depth below the AMV.

4.3. Mud extrusion resulting from density-inversion driven by gas exsolution

Once mud is generated at depth, it is necessary to understand how it is transferred to the surface. Modeling shows that mud ascent time is proportional to mud viscosity. Taking mud overpressure into account improves the convergence of 1D and 2D results (Figure 11). Similar values of velocity were obtained by Collignon et al. (2018b) who calculated flow rates depending on pipe radius, particle size and density and the type of gas for equivalent viscosities. One-dimensional extrapolation allows to test viscosities closer to those of sedimentary rocks, which was not possible on the 2D simulations due to time limitations. It would take approximately 100 years for the mud generated at the AMV location to rise to the surface if mud was only transported through density inversion and mud overpressure. The link between 2D results and the extrapolation in 1D may not straightforward. The extrapolation in 1D is made over 6 orders of magnitude of viscosities and compared to only two 2D control points. The relationship between mud remobilization and the host sediment viscosity may not be a linear process when dealing with high values of μ. Therefore, the results have to be addressed with caution. Nevertheless, some MVs display very slow extrusion rates, such as the Kotyrdag (onshore Azerbaijan), that extrudes high viscosity and slightly wet mud with an estimated rate of 0.02 m/day (Dupuis, 2017), in other words 2.3×10^{-7} m/s, which is the order of magnitude obtained from our modeling.

The presence of a preexisting conduit in our simulations modifies the extrusion time, but it reduces the extrusion rate as a smaller volume of mud is able to rise through the sedimentary column. One-dimensional calculations considering fracture radius show that the extrusion time is close to 10,000 years for $\mu = 10^{12}$ kPa.s. The simulations shown here do not address multi-phase flow, gas being only considered in the mass-density calculation. If free-gas was able to flow directly through the fracture, it may be able to fracture and/or damage shallower sediments, forming a secondary mud generation zone. This was observed at Lusi, where the BJP-1 well transferred overpressured fluids charged with gas to shallower and more fragile strata, triggering hydrofractures and mud generation (Tingay et al., 2008; Tingay et al., 2015).

In contrast to our numerical model in which mud ascent occurs along a unique wide fracture, field work reported by Roberts et al. (2010) seems to indicate that mud volcano conduits rather consist of an intricate and complex fractured volume with detached and rotated blocks. Roberts et al. (2010) explain their observations by the rising of overpressured and low-density mud that generates and propagates fractures as it rises, slowly opening its way up to the surface. Thus, the 2D simulations should rather compute the progressive opening of fractures as mud overpressure increases due to gas expansion. This would imply a combination of solid-rock mechanics and fluid mechanics that represents a complete field of research in modeling and computation, notably applied to hydrofracturing issues in well bores (Mainguy & Longuemare, 2002; Wu & Olson, 2015). The Lusi catastrophe allowed to monitor the initiation of a mud volcano formation. From the analysis of drilling reports, and notably records on the expelled gas, drilling mud losses and drilling mud pressure, Tingay et al. (2017) show that 24-48 hours separate the moment when free-gas was detected at the bottom of the well, and the moment when the mud extruded at the surface. Therefore, gas-driven mud generation and transport seem to occur very fast. Our model points to a transport duration of 100 years to cross the 3000 meters of strata separating the mud source from the surface but through the sole density inversion driven by gas expansion. The impact of gas expansion on overpressure and on rock failure is not explored but is expected to reduce significantly the time for extrusion. Besides, this combination of processes would imply a similar plumbing system as the one described by Roberts et al. (2010).

Another limitation of the current model is that the influence of gas exsolution on mud rheology was not accounted for. The presence of gas and liquids in the mud are known to strongly affect its viscosity (Kopf, 2002; Mazzini & Etiope, 2017). Collignon et al. (2018b) and Zoporowski & Miller (2009) both have considered a dynamic viscosity in their simulations and shows that the contrast between mud viscosity and the viscosity of the surrounding rock increases flow rates. Modeling results of Collignon et al. (2018b) demonstrated that the feeding pipe of the Lusi MV has to be smaller than 1.5 m radius in order to match its maximal mud discharge, when our model displays very long extrusion time for small fractures. Thus, the integration of a dynamic viscosity depending on gas content would certainly increase the velocity of the extrusion process in our model. It will also allow to study the effect of low-viscosity layers, for instance containing evaporites like the ASF. Besides, the gas mass-density was considered negligible in the calculation of the mud mass-density. However, gas mass-density depends on the pressure and temperature conditions, and represents 1/5 of the water mass-density at 35 MPa and 50 °C.

Finally, the code of Tryggvason (2012) was developed to answer fluid mechanics issues. Working with values corresponding to a geological background leads to very long calculation time due to computing limitations arising from the resolution method. Therefore, the code should be improved or another resolution method should be explored in order to run 2D simulations with parameters fitting the geological reality over shorter periods of time.

The sole effect of gas expansion on the mud mass-density is thus able to drive mud ascent up to the seafloor. The process may be accelerated if the influence of gas exsolution and expansion on mud viscosity and of fracture propagation ahead of the rising mud are accounted for. This modeling work resulted in extrusion rates of the same order of magnitude that what has been observed on MVs extruding high viscosity mud.

4.4. Towards a quantitative formation model for the Absheron mud volcano

The conceptual formation model for the AMV presented in Blouin et al. (2019a) was improved by integrating the main findings of Blouin et al. (2019b) and of the numerical models. This allows to move from a purely qualitative model, to a semi-quantitative one including the formation dynamics as a function of the main physical parameters controlling the mud volcano formation: ratio of overpressure to vertical effective stress, dissolved methane concentration and degree of gas saturation. The updated formation model is composed of 7 different phases shown in the different panels of Figure 13:

Phase 1 - At 3.4 Ma, end of the rapid deposition of the Productive Series (over 3.5 km in 2 My) above the gas-mature Maykop Formation that generated hydrocarbons diffusing slowly through the sedimentary column (Figure 13a). The Maykop Formation started generating gas during the Late Miocene in the Shah Deniz region located in a structural setting comparable to Absheron (figure 2.9 in Alizadeh et al., 2017). Moreover, the deposition of the Anhydritic Surakhany Formation provided an efficient seal allowing a slow and uniform overpressure build-up in the Productive Series generated by high sedimentation rates.

Phase 2 – At 0.7 Ma, the growth rate of the Absheron fold increased significantly. Methane circulation was therefore focused into the faulted core of the anticline (Figure 13b). The difference of overburden between the anticline and adjacent syncline generated an overpressure gradient leading to overpressure build-up against the sealing faults (Figure 13b). Besides, at the anticline crest, the vertical effective stress σ'_v is lower than on the flanks due to reduced overburden thickness. Thus, overpressure generation and transmission as well as low σ'_v at the crest increased the $\Delta u / \sigma'_v$ ratio.

Phase 3 –At ≈ 0.6 Ma, $\Delta u / \sigma'_v$ reached the hydro-fracturing threshold of 0.7 (Figure 13c), allowing hydrofracturing. This led to a local decrease of overpressure through fluid dissipation and triggered methane exsolution where the dissolved-methane concentration reached the methane solubility (Henry’s law; Figure 13c). For a gas saturation higher than 0.38, the sediment lost its preconsolidation pressure leading to mud generation (Figure 13c).

Phase 4 – The presence of gas bubbles in the mud significantly reduced its mass-density and its viscosity (Figure 13g). Therefore, the gassy mud started to rise along the open fractures. As gas bubbles moved up, they expanded (following Boyles’s law), hence increasing gas saturation and decreasing the mud mass-density and viscosity (Figure 13g). Thus, mud velocity increased as bubbles expanded. Gas expansion maintained the overpressure as mud rose along fractures, leading to a critical value of $\Delta u / \sigma'_v$ and to fracture propagation towards the surface (Figure 13g). This stage should have happened over a short period of time, ranging from hours to days.

Phase 5 – After several days, the fractured “pipe” connected the mud generation zone, where gas exsolution was still damaging sediments, with the seafloor (Figure 13d). First mud extrusion happened at the seafloor leading to the progressive formation of the extrusive edifice, while mud slowly degassed in the water column (Figure 13d). This direct hydraulic connection prevented overpressure from building up again at depth as it was directly transmitted to the surface (Figure 13d), thus preventing gas exsolution from stopping. At depth, the extrusion of remobilized mud slowly led to roof collapse, progressively forming what is known as a “depletion zone” (Dupuis et al., 2019; Kirkham et al., 2017; Stewart & Davies, 2006).

Phase 6 – After several years, multiple mud extrusion episodes reached the surface as the depletion zone became bigger along with the collapse of the overlying strata, forming a giant mud shield at the seafloor (Figure 13e). The AMV then entered a quiescent phase. Overpressure was not maintained high enough to keep fractures open and overpressure built up again along the sealing faults, preventing further gas exsolution (Figure 13e).

Phase 7 – Present day geometry, after multiple phases of quiescence and activity, creating a complex interdigitated geometry where normal sedimentation predominates during quiescent phases of the volcano. When $\Delta u / \sigma'_v$ reaches the fracture opening threshold, further depletion happens in the source, enhancing collapse, while more mud is extruded at the seafloor during the active phases (Figure 13f).

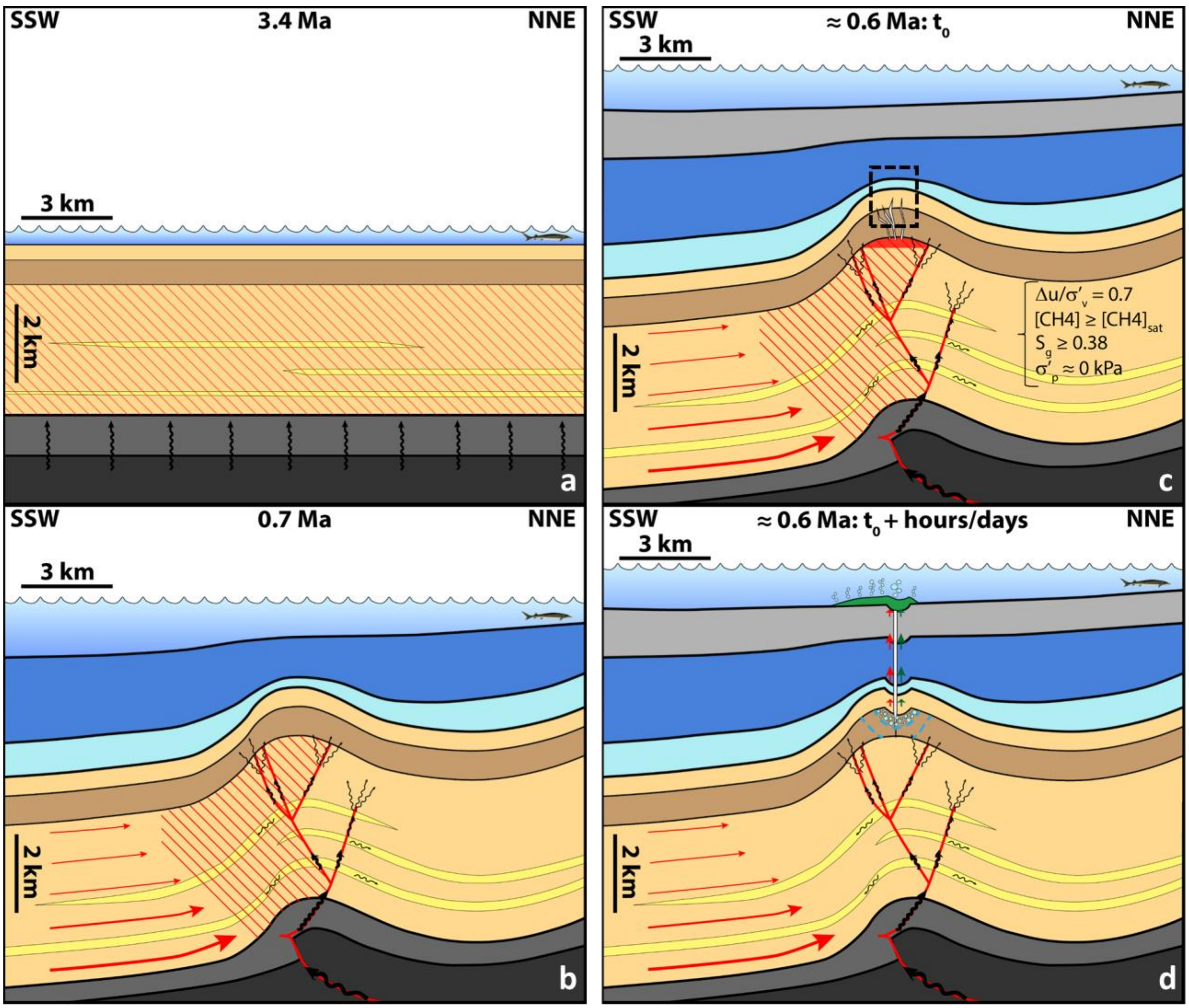

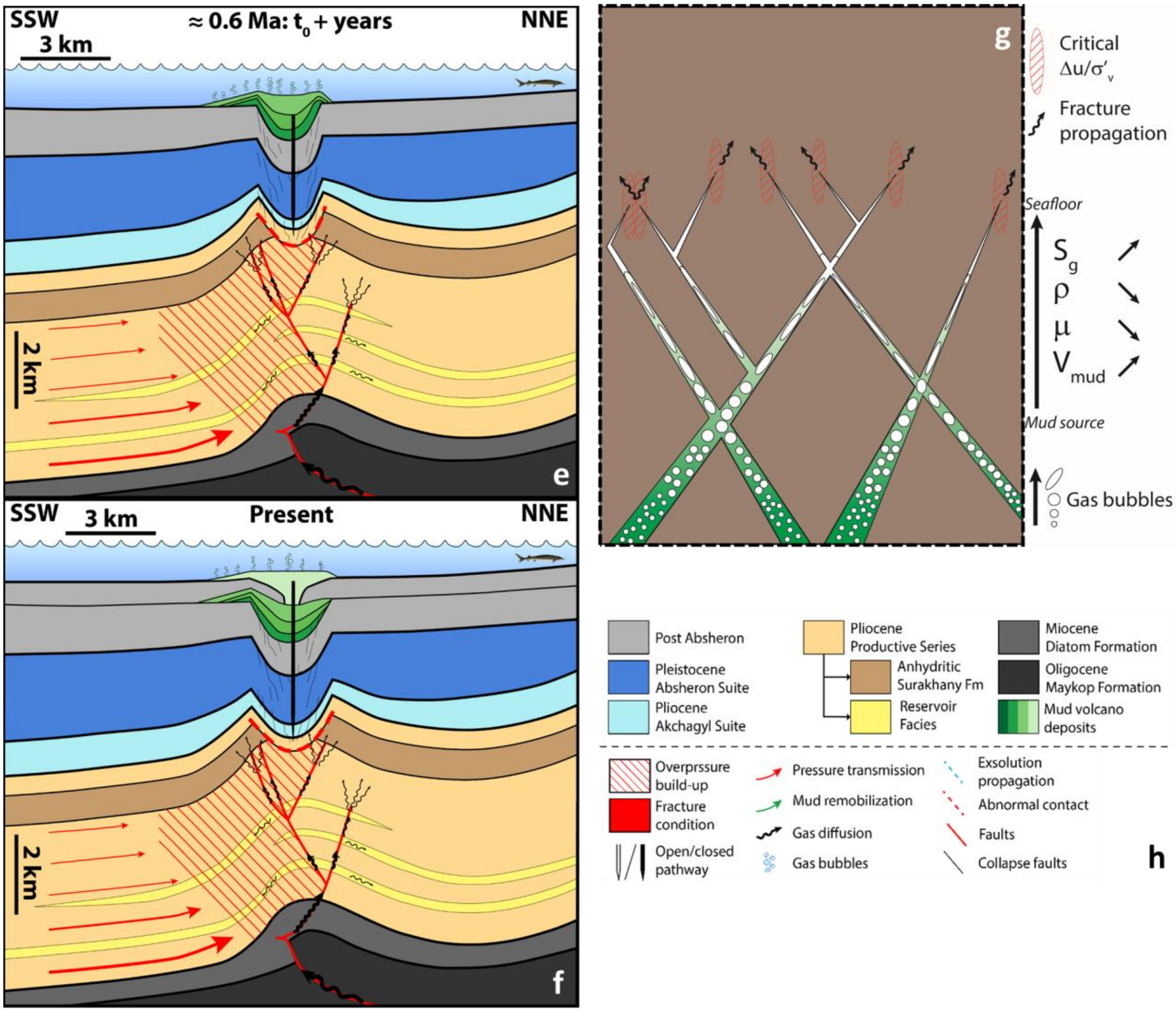

Figure 13: Formation model for the Absheron mud volcano based on in situ observations and measurements, sediment analysis, laboratory testing and mud generation and remobilization numerical modeling. Details of the different stages displayed in a, b, c, d, e, and f and g are in the text. g is a zoom corresponding to black dotted rectangle in c, and shows the processes involved in of mud remobilization towards the surface. h: legend corresponding to a, b, c, d, e and f.

5. Conclusion

This study explored the possibility of simulating mud generation and extrusion processes through numerical modeling based on simplified physical principles. The ultimate goal is to simulate the complete formation of the Absheron Mud Volcano (AMV) and to quantify the overpressure conditions and methane concentration that led to the present structure. A first model, considering 2D-diffusion laws (Darcy's law and Fick's law) was used to explain the location of the AMV as well as the conditions required to generate fluid mud from stratified solid sediments. The second model applies a fluid mechanics approach to test whether the sole impact of gas expansion on the mud density can lead to mud extrusion. The main results are:

1- The 2D-diffusion model showed that using sedimentation rates corrected from compaction to calculate overpressure in the deep basin and considering the low-permeability Anhydritic Surakhany Formation and sealing faults as flow baffles, critical fracture conditions are obtained at the crest of the Absheron anticline, below the ASF, where the depleted area was observed by Blouin et al. (2019).

2- A methane concentration of 5550 mM, imposed at the base of the fault network considered as permeable in the vertical direction creates the conditions for triggering gas exsolution and subsequent loss in preconsolidation pressure showing that liquid mud is generated at depth.

3- Mud ascent up to the seafloor through the sole density-inversion provoked by gas expansion is possible over a period of 100 years minimum. This period of time for extrusion corresponds to extrusion rates measured at particular MVs.

4- To accelerate the process, additional parameters such as non-constant viscosity and the upward propagation of fracture as consequences of gas expansion have to be considered.

5- The results allow going from a purely conceptual formation model to a semi-quantitative model considering dynamics of the processes involved and quantification of the main controlling physical parameters.

We show that simple physical models integrating realistic geological and hydro-mechanical parameters and behavior of sediments are able to reproduce the conditions that initiated the formation of the Absheron Mud Volcano. We simulated the key processes inferred from the available dense dataset and from the present geometry that were described in the conceptual model in Blouin et al. (2019). A dense and high-quality dataset is paramount to complete such models using the same methodology on other mud volcanoes located in similar contexts.

Acknowledgments, Samples, and Data

This study was realized in the scope of the PhD of Arthur Blouin under the joint direction of the Pau University (UPPA), Ifremer and Total S.A. To access the SeCoV3 software and output of the different presented simulations and calculations, please directly download it here https://doi.org/10.6084/m9.figshare.12052965.v2.

References

Abreu, V., & Nummedal, D. (2007). Miocene to Quaternary Sequence Stratigraphy of the South and Central Caspian Basins. *AAPG Studies in Geology*, *55*, 65–86. https://doi.org/10.1306/1205845St553000

Alizadeh, A. A., Guliyev, I. S., Kadirov, F. A., & Eppelbaum, L. V. (2017). *Geosciences of Azerbaijan Volume II : Economic Geology and Applied Geophysics* (Vol. II). Basel: Springer International Publishing Switzerland. https://doi.org/10.1007/978-3-319-40493-6

Allen, M. B., Jones, S., Ismail-Zadeh, A., Simmons, M., & Anderson, L. (2002). Onset of subduction as the cause of rapid Pliocene-Quaternary subsidence in the South Caspian basin. *Geology*, *30*(9), 775–778. https://doi.org/10.1130/0091-7613(2002)030<0775:OOSATC>2.0.CO;2

Battani, A., Prinzhofer, A., Deville, E., & Ballentine, C. J. (2010). Trinidad Mud Volcanoes: The Origin of the Gas. *Shale Tectonics: AAPG Memoir*, *93*, 225–238.

https://doi.org/10.1306/13231317M933427

Blouin, A. (2019). *Formation de boue à partir de sédiments stratifiés dans un contexte de volcanisme de boue: le rôle du gaz*. Université de Pau et des Pays de l'Adour.

Blouin, A., Imbert, P., Sultan, N., & Callot, J. (2019). Evolution model for the Absheron mud volcano : from in - situ observations to numerical modeling. *Journal of Geophysical Research: Earth Surface*, *124*(3), 766–794. https://doi.org/10.1029/2018JF004872

Blouin, A., Sultan, N., Callot, J., & Imbert, P. (2019). Sediment damage caused by gas exsolution: a key mechanism for mud volcano formation. *Engineering Geology*, *263*.

Bredehoeft, J. D., Djevanshir, R. D., & Belitz, K. R. (1988). Lateral fluid flow in a compacting sand-shale sequence: South Caspian basin. *American Association of Petroleum Geologists Bulletin*, *72*(4), 416–424. https://doi.org/10.1306/703C9A1E-1707-11D7-8645000102C1865D

Brown, K. M. (1990). The nature and hydrogeologic significance of mud diapirs and diatremes for accretionary systems. *Journal of Geophysical Research*, *95*(B6), 8969. https://doi.org/10.1029/JB095iB06p08969

Caine, J. S., Evans, J. P., & Forster, C. B. (1996). Fault zone architecture and permeability structure. *Geology*, *24*(11), 1025–1028. https://doi.org/https://doi.org/10.1130/0091-7613(1996)024<1025:FZAAPS>2.3.CO;2

Collignon, M., Mazzini, A., Schmid, D. W., & Lupi, M. (2018). Modelling fluid flow in active clastic piercements: Challenges and approaches. *Marine and Petroleum Geology*, *90*, 157–172. https://doi.org/10.1016/j.marpetgeo.2017.09.033

Collignon, M., Schmid, D. W., Galerne, C., Lupi, M., & Mazzini, A. (2018). Modelling fluid flow in clastic eruptions: Application to the Lusi mud eruption. *Marine and Petroleum Geology*, *90*, 173–190. https://doi.org/10.1016/j.marpetgeo.2017.08.011

Contet, J., & Unterseh, S. (2015). Multiscale site investigation of a giant mud-volcano offshore Azerbaijan - Impact on subsea field development. *Offshore Technology Conference, OTC-25864*(Mv), 1–10. https://doi.org/10.4043/25864-MS

DeGroot, D. J., Lunne, T., & Tjelta, T. I. (2010). Recommended best practise for geotechnical site characterisation of cohesive offshore sediments. In S. Gourvenec & D. White (Eds.), *Frontiers in Offshore Geotechnics II* (pp. 33–57). Perth, Australia: CRC Press, Taylor & Francis Group.

Deville, E. (2009). Mud Volcano Systems. In N. Lewis & A. Moretti (Eds.), *Volcanoes: Formation, Eruptions and Modelling* (pp. 95-125 (404)). Nova Science Publishers.

Deville, Eric, Guerlais, S. H., Lallemant, S., & Schneider, F. (2010). Fluid dynamics and subsurface sediment mobilization processes: An overview from Southeast Caribbean. *Basin Research*, *22*(4), 361–379. https://doi.org/10.1111/j.1365-2117.2010.00474.x

Diaconescu, C. C., Kieckhefer, R. M., & Knapp, J. H. (2001). Geophysical evidence for gas hydrates in the deep water of the South Caspian Basin, Azerbaijan. *Marine and Petroleum Geology*, *18*(2), 209–221. https://doi.org/10.1016/S0264-8172(00)00061-1

Dimitrov, L. I. (2002). Mud volcanoes-the most important pathway for degassing deeply buried sediments. *Earth-Science Reviews*, *59*(1–4), 49–76. https://doi.org/10.1016/S0012-8252(02)00069-7

Duan, Z., & Mao, S. (2006). A thermodynamic model for calculating methane solubility, density and gas phase composition of methane-bearing aqueous fluids from 273 to 523 K and from 1 to 2000 bar. *Geochimica et Cosmochimica Acta*, *70*(13), 3369–3386. https://doi.org/10.1016/j.gca.2006.03.018

Dugan, B., & Flemings, P. (2000). Overpressure and fluid flow in the new jersey continental slope: implications for slope failure and cold seeps. *Science (New York, N.Y.)*, *289*(July), 288–291. https://doi.org/10.1126/science.289.5477.288

Dupuis, M. (2017). *Processus de mise en place et évolution des systèmes de volcans de boue*. Université Lille 1 - Sciences et technlogies.

Dupuis, M., Imbert, P., Odonne, F., & Vendeville, B. (2019). Mud volcanism by repeated roof collapse : 3D architecture and evolution of a mud volcano cluster o ff shore Nigeria. *Marine and Petroleum Geology*, *110*(July), 368–387. https://doi.org/10.1016/j.marpetgeo.2019.07.033

Egan, S. S., Mosar, J., Brunet, M.-F., & Kangarli, T. (2009). Subsidence and uplift mechanisms within the South Caspian Basin: insights from the onshore and offshore Azerbaijan region. *Geological Society, London, Special Publications*, *312*(1), 219–240. https://doi.org/10.1144/SP312.11

Esrig, M. I., & Kirby, R. C. (1977). Implications of gas content for predicting the stability of submarine slopes. *Marine Geotechnology*, *2*(1–4), 81–100. https://doi.org/10.1080/10641197709379771

Etiope, G., Feyzullayev, A., & Baciu, C. L. (2009). Terrestrial methane seeps and mud volcanoes: A global perspective of gas origin. *Marine and Petroleum Geology*, *26*(3), 333–344. https://doi.org/10.1016/j.marpetgeo.2008.03.001

Evans, J. P., Forster, C. B., & Goddard, J. V. (1997). Permeability of fault-related rocks , and implications for hydraulic structure of fault zones. *Journal of Structural Geology*, *19*(11), 1393–1404. https://doi.org/https://doi.org/10.1016/S0191-8141(97)00057-6

Forte, A. M., & Cowgill, E. (2013). Late Cenozoic base-level variations of the Caspian Sea: A review of its history and proposed driving mechanisms. *Palaeogeography, Palaeoclimatology, Palaeoecology*, *386*, 392–407. https://doi.org/10.1016/j.palaeo.2013.05.035

Furbish, D. J. (1997). *Fluid Physics in Geology*. New York: Oxford University Press.

Gautherot, T., Total, S. A., Bakirov, S., Upstream, S., & International, M. (2015). Absheron Field – ABX-2 Exploration Drilling Challenges and Realizations Return to Absheron field, (June 2009), 4–6.

Gisler, G. (2009). Simulations of the explosive eruption of superheated fluids through deformable media. *Marine and Petroleum Geology*, *26*(9), 1888–1895. https://doi.org/10.1016/j.marpetgeo.2008.12.006

Gordon, D. S., & Flemings, P. B. (1998). Generation of overpressure and compaction-driven fluid flow in a Plio-Pleistocene Eugene Island 330 , offshore Louisiana. *Basin Research*, *10*, 177–196.

Grauls, D. J., & Baleix, J. M. (1994). Role of overpressures and in situ stresses in fault-controlled hydrocarbon migration : a case study. *Marine and Petroleum Geology*, *11*(6), 734–742.

Green, T., Abdullayev, N., Hossack, J., Riley, G., & Roberts, A. M. (2009). Sedimentation and subsidence in the South Caspian Basin, Azerbaijan. *Geological Society, London, Special Publications*, *312*(1), 241–260. https://doi.org/10.1144/SP312.12

Grosjean, Y., Zaugg, P., Gaulier, J.-M., & Total S.A. (2009). Burial Hydrodynamics and Subtle Hydrocarbon Trap Evaluation : From the Mahakam Delta to the South Caspian Sea. *International Petroleum Technology Conference Held in Doha, Qatar, 7-9 December 2009*, 1–12.

Guliyev, I., Aliyeva, E., Huseynov, D., Feyzullayev, A., & Mamedov, P. (2011). Hydrocarbon Potential of Ultra Deep Deposits in the South Caspian Basin. In *AAPG European Region Annual Conference* (Vol. 1, p. 66). Kiev, Ukraine.

Henry, P., Guglielmi, Y., Gout, C., Castilla, R., Dick, P., Donzé, F., et al. (2019). Strain and flow pathways in a shale fault zone : An in-situ test of fault seal integrity. In *Fifth International Conference on Fault and Top Seals* (pp. 8–12). Palermo, Italy: EAGE Publications.

Hight, D. W., Hamza, M. M., & El Sayed, A. S. (2002). Engineering characterization of the Nile Delta clays. In A. Nakase & T. Tsuchida (Eds.), *Coastal geotechnical engineering in practice* (pp. 149–162). Lisse, the Netherlands: Swets & Zeitlinger.

Hinds, D. J., Aliyeva, E., Allen, M. B., Davies, C. E., Kroonenberg, S. B., Simmons, M. D., & Vincent, S. J. (2004). Sedimentation in a discharge dominated fluvial-lacustrine system: The Neogene Productive Series of the South Caspian Basin, Azerbaijan. *Marine and Petroleum Geology*, *21*(5), 613–638. https://doi.org/10.1016/j.marpetgeo.2004.01.009

Hubbert, M. K. (1937). Theory of scale models as applied to the study of geologic structures. *Bulletin of the Geological Society of America*, *48*, 1459–1520.

Hustoft, S., Dugan, B., & Mienert, J. (2009). Effects of rapid sedimentation on developing the Nyegga pockmark field: Constraints from hydrological modeling and 3-D seismic data, offshore mid-Norway. *Geochemistry, Geophysics, Geosystems*, *10*(6).

https://doi.org/10.1029/2009GC002409

Imbert, P., Geiss, B., & Fatjó de Martín, N. (2014). How to evacuate 10 km3 of mud: Saturate with gas and decrease the pressure! *Geo-Marine Letters*, *34*(2–3), 199–213. https://doi.org/10.1007/s00367-014-0357-3

Inan, S., Namik Yalçin, M., Guliev, I. S., Kuliev, K., & Akper Feizullayev, A. (2002). Deep petroleum occurrences in the Lower Kura Depression, South Caspian Basin, Azerbaijan: an organic geochemical and basin modeling study. *Marine and Petroleum Geology*, *14*(7–8), 731–762. https://doi.org/10.1016/s0264-8172(97)00058-5

Javanshir, R. J., Riley, G. W., Duppenbecker, S. J., & Abdullayev, N. (2015). Validation of lateral fluid flow in an overpressured sand-shale sequence during development of Azeri-Chirag-Gunashli oil field and Shah Deniz gas field: South Caspian Basin, Azerbaijan. *Marine and Petroleum Geology*, *59*, 593–610. https://doi.org/10.1016/j.marpetgeo.2014.07.019

Jeong, S. W. (2013). Determining the viscosity and yield surface of marine sediments using modified Bingham models. *Geosciences Journal*, *17*(3), 241–247. https://doi.org/10.1007/s12303-013-0038-7

Kirkham, C., Cartwright, J., Hermanrud, C., & Jebsen, C. (2017). The genesis of mud volcano conduits through thick evaporite sequences. *Basin Research*, 1–20. https://doi.org/10.1111/bre.12250

Kopf, A. J. (2002). Significance of mud volcanism. *Reviews of Geophysics*, *40*(2), 1005. https://doi.org/10.1029/2000RG000093

Kvalstad, T. J., Andresen, L., Forsberg, C. F., Berg, K., Bryn, P., & Wangen, M. (2005). The Storegga slide: Evaluation of triggering sources and slide mechanics. *Marine and Petroleum Geology*, *22*(1-2 SPEC. ISS.), 245–256. https://doi.org/10.1016/j.marpetgeo.2004.10.019

Lafuerza, S., Sultan, N., Canals, M., Lastras, G., Cattaneo, A., Frigola, J., et al. (2012). Failure mechanisms of Ana Slide from geotechnical evidence , Eivissa Channel , Western Mediterranean Sea. *Marine Geology*, *307–310*, 1–21. https://doi.org/10.1016/j.margeo.2012.02.010

Lawrence, G. W. M., & Cartwright, J. A. (2010). The stratigraphic and geographic distribution of giant craters and remobilised sediment mounds on the mid Norway margin , and their relation to long term fluid flow Slid e W. *Marine and Petroleum Geology*, *27*(4), 733–747. https://doi.org/10.1016/j.marpetgeo.2009.10.012

Locat, J., & Demers, D. (2008). Viscosity, yield stress, remolded strength, and liquidity index relationships for sensitive clays. *Canadian Geotechnical Journal*, *25*(4), 799–806. https://doi.org/10.1139/t88-088

Lunne, T., Berre, T., Strandvik, S., Andersen, K. H., & Tjelta, T. I. (2001). Deepwater sample disturbance due to stress relief. In *Proceedings of the 1st Annual Offshore Technology*

Conference (pp. 64–85). Houston, Texas.

Mainguy, M., & Longuemare, P. (2002). Coupling Fluid Flow and Rock Mechanics : Formulations of the Partial Coupling between Reservoir and Geomechanical Simulators. *Oil & Gas Science and Technology*, *57*(4), 355–367.

Mazzini, A., & Etiope, G. (2017). Mud volcanism: An updated review. *Earth-Science Reviews*, *168*, 81–112. https://doi.org/10.1016/j.earscirev.2017.03.001

Mazzini, Adriano, Etiope, G., & Svensen, H. (2012). A new hydrothermal scenario for the 2006 Lusi eruption, Indonesia. Insights from gas geochemistry. *Earth and Planetary Science Letters*, *317–318*(May 2006), 305–318. https://doi.org/10.1016/j.epsl.2011.11.016

Morley, C. K., von Hagke, C., Hansberry, R., Collins, A., Kanitpanyacharoen, W., & King, R. (2017). Review of major shale-dominated detachment and thrust characteristics in the diagenetic zone: Part I, meso- and macro-scopic scale. *Earth-Science Reviews*, *172*(May). https://doi.org/10.1016/j.earscirev.2017.07.019

Morton, A., Allen, M., Simmons, M., Spathopoulos, F., Still, J., Hinds, D., et al. (2003). Provenance patterns in a neotectonic basin: Pliocene and quaternary sediment supply to the South Caspian. *Basin Research*, *15*(3), 321–337. https://doi.org/10.1046/j.1365-2117.2003.00208.x

Mourgues, R., Bureau, D., Bodet, L., Gay, A., & Gressier, J. B. (2012). Formation of conical fractures in sedimentary basins: Experiments involving pore fluids and implications for sandstone intrusion mechanisms. *Earth and Planetary Science Letters*, *313–314*(1), 67–78. https://doi.org/10.1016/j.epsl.2011.10.029

Mukherjee, S., Talbot, C. J., & Koyi, H. A. (2010). Viscosity estimates of salt in the Hormuz and Namakdan salt diapirs , Persian Gulf. *Geology Magazine*, *147*(4), 497–507. https://doi.org/10.1017/S001675680999077X

Nermoen, A., Galland, O., Jettestuen, E., Fristad, K., Podladchikov, Y., Svensen, H., & Malthe-Srenssen, A. (2010). Experimental and analytic modeling of piercement structures. *Journal of Geophysical Research: Solid Earth*, *115*(10), 1–15. https://doi.org/10.1029/2010JB007583

Odonne, F., Imbert, P., Dupuis, M., Aliyev, A. A., Abbasov, O. R., Baloglanov, E. E., et al. (2020). Mud volcano growth by radial expansion : Examples from onshore Azerbaijan. *Marine and Petroleum Geology*, *112*(September 2019), 104051. https://doi.org/10.1016/j.marpetgeo.2019.104051

Opara, A. I. (2011). ESTIMATION OF MULTIPLE SOURCES OF OVERPRESSURES USING VERTICAL EFFECTIVE STRESS APPROACH : CASE STUDY OF THE NIGER DELTA , NIGERIA. *Petroleum & Coal*, *53*(4), 302–314.

Osborne, M. J., & Swarbrick, R. E. (1997). Mechanisms for Generating Overpressure in Sedimentary Basins : A Reevaluation 1. *AAPG Bulletin*, *6*(6), 1023–1041.

PCDM. (2018). Calculateur principal, DATARMOR. Retrieved August 27, 2019, from https://wwz.ifremer.fr/pcdm/Equipement

Priest, J. A., Clayton, C. R. I., & Rees, E. V. L. (2014). Potential impact of gas hydrate and its dissociation on the strength of host sediment in the Krishna-Godavari Basin. *Marine and Petroleum Geology*, *58*(PA), 187–198. https://doi.org/10.1016/j.marpetgeo.2014.05.008

Riboulot, V., Cattaneo, A., Sultan, N., Garziglia, S., Ker, S., Imbert, P., & Voisset, M. (2013). Sea-level change and free gas occurrence influencing a submarine landslide and pockmark formation and distribution in deepwater Nigeria. *Earth and Planetary Science Letters*, *375*, 78–91. https://doi.org/10.1016/j.epsl.2013.05.013

Roberts, K. S., Davies, R. J., & Stewart, S. A. (2010). Structure of exhumed mud volcano feeder complexes, Azerbaijan. *Basin Research*, *22*(4), 439–451. https://doi.org/10.1111/j.1365-2117.2009.00441.x

Schneider, F., Pagel, M., & Hernandez, E. (2004). Basin Modeling in a Complex Area: Example from the Eastern Venezuelan Foothills. In R. Swennen, F. Roure, & J. W. Granath (Eds.), *Deformation, fluid flow, and reservoir appraisal in foreland fold and thrust belts* (pp. 357–369). AAPG Hedberg Series. https://doi.org/10.1306/1025700H1504

Sibson, R. H. (2003). Brittle-failure controls on maximum sustainable overpressure in different tectonic regimes. *American Association of Petroleum Geologists Bulletin*, *87*(6), 901–908. https://doi.org/10.1306/01290300181

Smith-Rouch, L. S. (2006). Oligocene-Miocene Maykop/Diatom Total Petroleum System of the South Caspian Basin Province, Azerbaijan, Iran, and Turkmenistan. *U.S. Geological Survey Bulletin*, *2201–I*, 27.

Stewart, S. A., & Davies, R. J. (2006). Structure and emplacement of mud volcano systems in the South Caspian Basin. *AAPG Bulletin*, *90*(5), 771–786. https://doi.org/10.1306/11220505045

Sultan, N., Savoye, B., Jouet, G., Leynaud, D., Cochonat, P., Henry, P., et al. (2010). Investigation of a possible submarine landslide at the Var delta front (Nice slope - SE France). *Canadian Geotechnical Journal*, *47*(4), 486–496.

Sultan, N., De Gennaro, V., & Puech, A. (2012). Mechanical behaviour of gas-charged marine plastic sediments. *Géotechnique*, *62*(9), 751–766. https://doi.org/10.1680/geot.12.OG.002

Tagiyev, M. F., Nadirov, R. S., Bagirov, E. B., & Lerche, I. (1997). Geohistory, thermal history and hydrocarbon generation history of the north-west South Caspian Basin. *Marine and Petroleum Geology*, *14*(4), 363–382. https://doi.org/10.1016/S0264-8172(96)00053-0

Tingay, M., Heidbach, O., Davies, R., & Swarbrick, R. (2008). Triggering of the Lusi mud eruption: Earthquake versus drilling initiation. *Geology*, *36*(8), 639–642. https://doi.org/10.1130/G24697A.1

Tingay, M., Manga, M., Rudolph, M. L., & Davies, R. (2017). An alternative review of facts, coincidences and past and future studies of the Lusi eruption. *Marine and Petroleum Geology*, (December). https://doi.org/10.1016/j.marpetgeo.2017.12.031

Tingay, M. R. P., Rudolph, M. L., Manga, M., Davies, R. J., & Wang, C.-Y. (2015). Initiation of the Lusi mudflow disaster. *Nature Geoscience*, *8*(7), 493–494. https://doi.org/10.1038/ngeo2472

Torrance, J. K. (2010). Shear resistance of remoulded soils by viscometric and fall-cone methods: a comparison for the Canadian sensitive marine clays. *Canadian Geotechnical Journal*, *24*(2), 318–322. https://doi.org/10.1139/t87-037

Tryggvason, G. (2011). Direct Numerical Simulations of Multiphase Flows: An Introduction. Retrieved September 24, 2019, from https://www3.nd.edu/~gtryggva/MultiphaseDNS/

Tryggvason, G, Scardovelli, R., & Zaleski, S. (2011). *Direct Numerical Simulations of Gas-Liquid Multiphase Flows*. Cambridge university press.

Tryggvason, Gretar. (2012). *A Front-tracking/Finite-Volume Navier-Stokes Solver for Direct Numerical Simulations of Multiphase Flows*.

Tryggvason, Gretar, Esmaeeli, A., Lu, J., & Biswas, S. (2006). Direct numerical simulations of gas / liquid multiphase flows Direct numerical simulations of gas / liquid multiphase flows. *Fluid Dynamics Research*, *38*, 660–681. https://doi.org/10.1016/j.fluiddyn.2005.08.006

Unterseh, S., & Contet, J. (2015). Integrated geohazards assessments offshore Azerbaijan, Caspian Sea. *Offshore Technology Conference*, *OTC-25911*(May), 1–8. https://doi.org/10.4043/25911-MS

Vincent, S. J., Davies, C. E., Richards, K., & Aliyeva, E. (2010). Contrasting Pliocene fluvial depositional systems within the rapidly subsiding South Caspian Basin; a case study of the palaeo-Volga and palaeo-Kura river systems in the Surakhany Suite, Upper Productive Series, onshore Azerbaijan. *Marine and Petroleum Geology*, *27*(10), 2079–2106. https://doi.org/10.1016/j.marpetgeo.2010.09.007

Wibberley, C. A. J., Yielding, G., & Di Toro, G. (2008). Recent advances in the understanding of fault zone internal structure: a review. *Geological Society, London, Special Publications*, *299*(1), 5–33. https://doi.org/10.1144/sp299.2

Wibberley, C. A. J., Gonzalez-Dunia, J., & Billon, O. (2017). Faults as barriers or channels to production-related flow: insights from case studies. *Petroleum Geoscience*, *23*(1), 134–147. https://doi.org/10.1144/petgeo2016-057

Woolsey, S., McCallum, M. E., & Schumm, S. A. (1975). Modeling of Diatreme Emplacement, 29–42.

Wu, K., & Olson, J. E. (2015). Simultaneous Multifracture Treatments : Fully Coupled Fluid Flow and Fracture Mechanics for Horizontal Wells. In *SPE Annual Technical Conference and Exhibition* (pp. 337–346). New Orleans: Society of Petroleum Engineers.

Zoporowski, A., & Miller, S. A. (2009). Modelling eruption cycles and decay of mud volcanoes. *Marine and Petroleum Geology*, *26*(9), 1879–1887. https://doi.org/10.1016/j.marpetgeo.2009.03.003